SCARF Annual Report 2018–2019

J Roddom (editor)

October 2022

Neither the Council nor the Laboratory accept any responsibility for loss or damage arising from the use of information contained in any of their reports or in any communication about their tests or investigations.
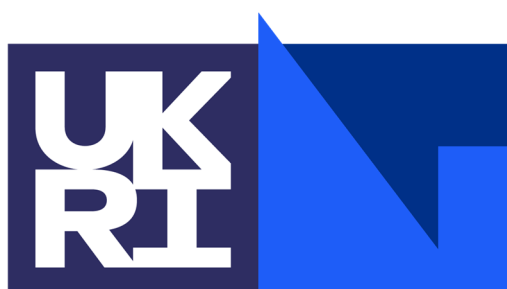
SCARF Annual Report 2018-2019

Version: 1.0

Date: 21/10/2021

Edited by Jon Roddom (jonathan.roddom@stfc.ac.uk) 01235 445141

Content written by the respective authors

Date	Revision	Changes
30/01/20	0.1	Initial document outline
28/08/20	0.2	Addition of scientific contributions
18/12/20	0.3	Reformatting and restructuring
29/04/21	0.4	Added Index of Figures
15/10/21	0.5	Minor corrections
21/10/21	1.0	Release version

Abstract

Annual Report on the Usage and Scientific Impact of the SCARF Service

Dissemination

This is a public document

SCARF Annual Report 2018-2019

1. SCARF SERVICE

SCARF is a High-Performance Cluster for STFC staff, Facilities (ISIS, DIAMOND, CLF) and their users and collaborators. The SCARF Service was started in 2004 and has been upgraded year-on-year and now represents a significant capital investment in High Performance Computing. Overall SCARF now has approximately 558 nodes providing nearly 12,000 CPU cores and 80TB memory, underpinned by 3PB of disk space (Details in Appendix A).

This report covers the year 2018-19 and outlines the research that SCARF has enabled.

SCARF Usage by Department

Each time a researcher uses the SCARF service the CPU time used is recorded. Jobs submitted to SCARF used 62 million CPU Hours during 2018-19.
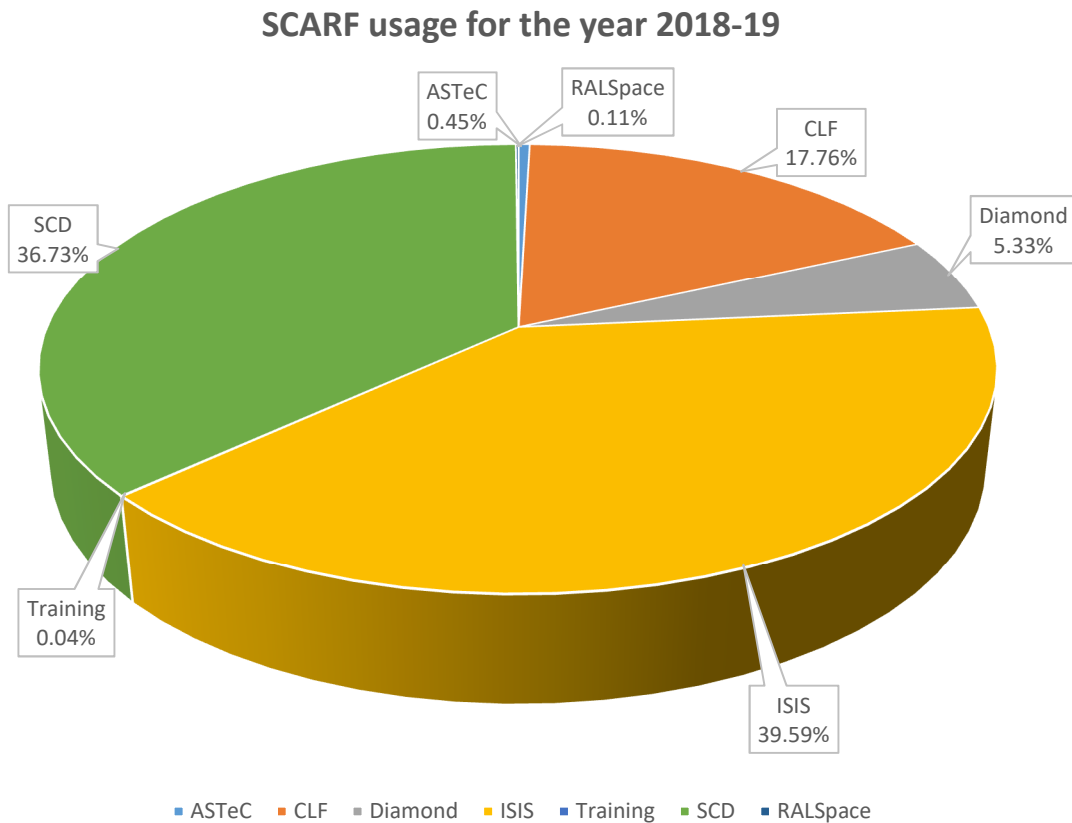
Figure 1: Pie chart showing percentage usage of SCARF, by department

It is clear from the usage chart that ISIS and Scientific Computing are by far the heaviest users of SCARF with CLF, still a significant consumer of resources, next. Diamond, whilst still a relatively small user of SCARF, has almost doubled its usage in the past year.
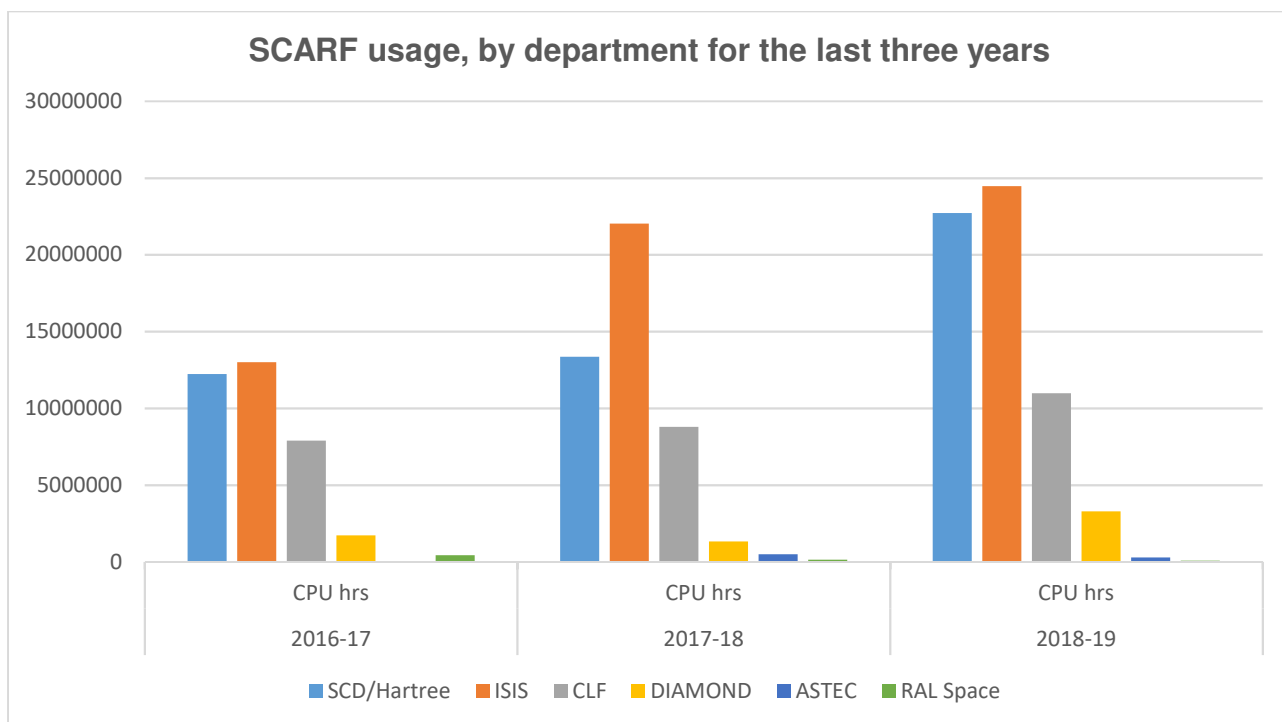
Figure 2: Graph showing SCARF usage by department, for the last three years

The table below shows the number of active users and their CPU usage for the last three years. There is no distinction made between STFC staff or external collaborators. We have included the Training accounts this year and while usage for this purpose is still small, it is an area of growth.

Department	2018-2019			2017-18			2016-17		
	Active Users	CPU hrs	%	Active Users	CPU hrs	%	Active Users	CPU hrs	%
SCD/Hartree	100	22709660	36.7	89	13366201	29	71	12229693	34.7
ISIS	73	24474255	39.6	79	22031658	47.7	61	12998062	36.8
CLF	53	10979295	17.8	60	8794903	19.1	56	7893198	22.4
DIAMOND	29	3294523	5.3	16	1320589	2.9	11	1717468	4.9
ASTEC	3	276944	0.4	2	496252.9	1.1	0	0	0
RAL Space	1	69460	0.1	1	133180.9	0.3	4	432680.9	1.2
Training	N/A	22828	0						
CCFE	0	0	0	0	0	0	0	0	0
PPD	0	0	0	0	0	0	3	15108.7	0.04
Totals	259	61826965	100	247	46142785	100	206	35286209	100

Figure 3: Table displaying detailed CPU usage from 2018-19 compared to 2016-17 and 2017-18

A significant amount of computational resource has been utilised on SCARF and Section 3 highlights some of the scientific achievements that have been made possible with it.

SCARF Availability

We aim to keep SCARF available to users as much as possible.

There was one significant unplanned interruption of service during this reporting period when a switch failure caused connectivity issues to the VMWare hypervisor pool. The failure occurred over the Christmas period but was fixed on the day that support staff returned.

There were some brief restrictions to the login nodes to allow for routine security patching but at least one login node was always available.

- A rolling reboot of login nodes for routine security patching was done in February and July
- In April, the switch that provides SCARF's uplink to the STFC network and the internet needed to be rebooted
- In June, head node scarf.rl.ac.uk was rebooted to resolve issues resulting from high load
- During the storage migration, individual users were asked not to login for a period of up to a day, but significant notice was given beforehand and where required the schedule was changed to suit the individual's needs.

SCARF Developments 2018-19

Major SCARF Developments are listed below. A more detailed list can be found in Appendix D.

- Continuation of the migration from RHEL6 and the move to SLURM
- Migration of all storage areas to the new Panasas instance
- Adoption of the Easybuild software building and installation framework for delivering applications software. Previously such software was compiled manually or using custom shell scripts.
- Commissioned a 2PB, Infiniband-connected GPFS fast scratch volume

Future Developments

- We plan to move Platform MPI to OpenMPI for SCARF's default MPI implementation. This is due to the rising costs associated with licensing Platform MPI and we feel that this move will provide similar features and performance whist reducing costs significantly.
- Further expansion of the GPFS storage system
- Moving to a new purchasing model for SCARF upgrades which will allow us to better align CPU and storage procurements

Help and Support

For any queries concerning the SCARF service, please email the SCARF Helpdesk scarf@hpc-support.rl.ac.uk

2. PUBLICATIONS AND PRESENTATIONS

The publications and presentations for research that made use of SCARF are a way of measuring the impact that SCARF itself has.

Publications

A list of publications is given in Section 5.

Presentations

Scientists have presented their work at 20 international conferences (See Section 5). This helps to demonstrate that the science enabled by SCARF is world class.

3. SCIENCE HIGHLIGHTS

Computational Chemistry studies into catalysts developed with the UK Catalysis Hub

Summary of ongoing work produced with the aid of SCARF

K. Butler

Scientific Computing, STFC

Calculations on the competitive adsorption of CO_2 and NO_2 on Superbase Ionic Liquids are now completed. These results complement experimental data from Manchester well and help provide kinetic/thermodynamic explanations for the observed loss of CO_2 uptake when the Benzim IL is exposed to NO_2 poisoning. A first draft of a paper originating from this data has now been prepared and should be submitted for publication soon.

Work on the $Ni_3Si_2O_5(OH)_4$ catalysts is still very much ongoing and is the focus of extensive experimental collaboration with Diamond scientists. Calculations are progressing as expected with complete IR simulations of the pristine and activated (defect) catalysts being completed, in addition to initial calculation on the activation of CO_2. Theoretical models that also include H_2 and MeOH are currently being investigated in coordination with further experimental studies.

The modelling component of the Pd substituted NiO catalyst is also progressing as planned. XAFs and DRIFTs results provided by Dr. Chris Parlett are informing the theoretical work, whereby the low-index surfaces of NiO are undergoing sequential Pd substitution in order to ascertain whether there is a thermodynamical basic for the observed level of Ni exchange.

E_V (eV) = 2.42 {2.37} E_V (eV) = 1.99 {2.02}
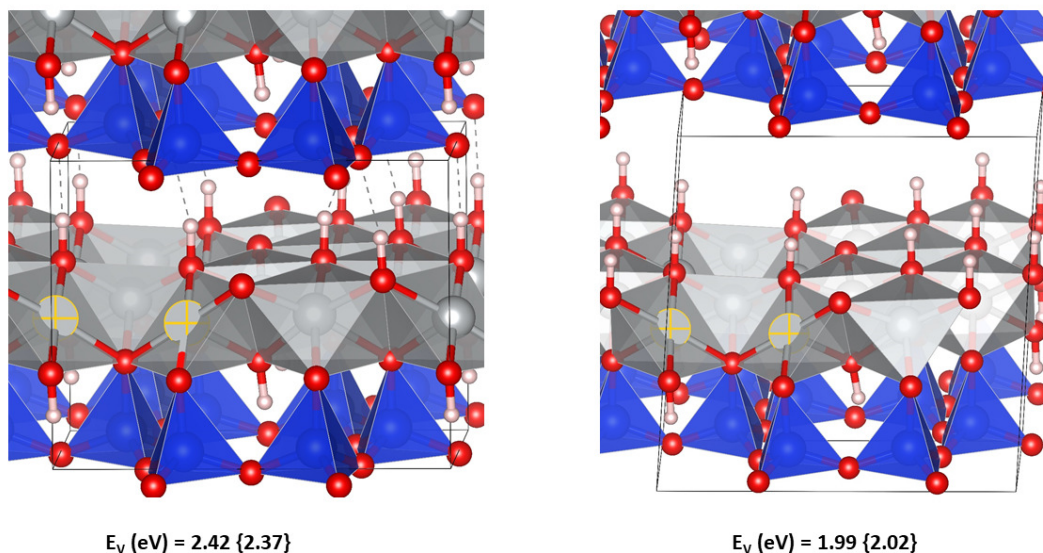
Figure 4: Phyllosilicate ((Ni3Si2O5(OH)4)) vacancy formation using empirical D3 (left) and the charge dependent dispersion method dDSC (right)

Finally, various models have been developed to locate an intermediate in the FAU catalysed N2O pathway, which has been seen experimentally in IR spectra produced by Prof. Beale and Dr. Negahdar. Early results point to the involvement of NO3 co-bound to the Cu1 of copper aluminate and a hydrogen from ammonia.

SuperSTEM and high-performance computing to study porous glasses

K. Butler

Scientific Computing, STFC
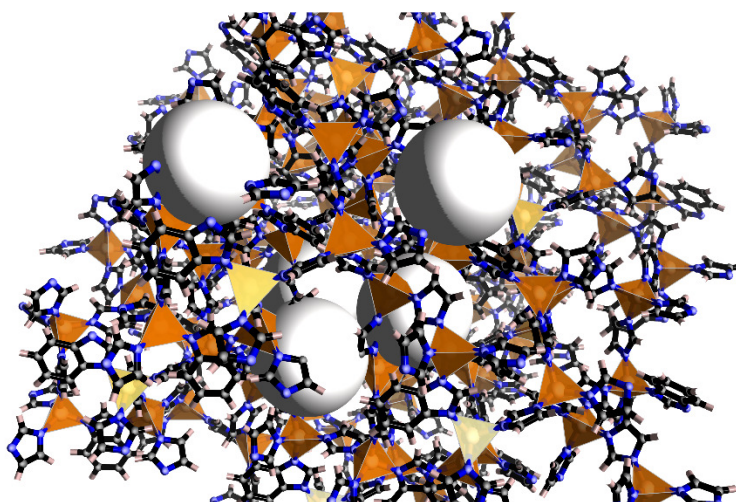
Figure 5: Porous hybrid organic-inorganic glass

Density functional theory (DFT) calculations have been used, with machine learning, to disentangle complex microscopy images of metal-organic-frameworks (MOFs) at unprecedented resolution. A collaboration between researchers in SCD and the University of Cambridge is leading the way in understanding mixing of different systems in these important new materials.

MOFs are a class of materials that were first reported in the late 1990s and have since then excited chemists with their unique combination of crystal structure and porosity, showing great potential for application in gas storage and separation, catalysis and recently electronic applications. Recently researchers also reported so called MOF-glasses, where porosity is retained but the structure loses long range crystal order, becoming amorphous, like a glass.

MOF glasses have fascinating properties and mixing of different compositions could potentially be utilised, just like in traditional silica glasses, to develop highly-tuanble materials. However, an understanding of how MOFs mix is currently in the early stages. Electron microscopy offers the possibility of imaging MOF glass mixtures and providing previously unobtainable levels of detail. However, understanding the images collected from electron microscopes on MOF glasses is extremely challenging.

DFT calculations performed on SCARF, combined with machine learning models have provided a new route to analysing the images collected at the ePSIC electron microscope at Diamond Light Source. These analyses have resulted in a number of high-impact publications:

Understanding vibrational entropy with neutrons and high-performance computing
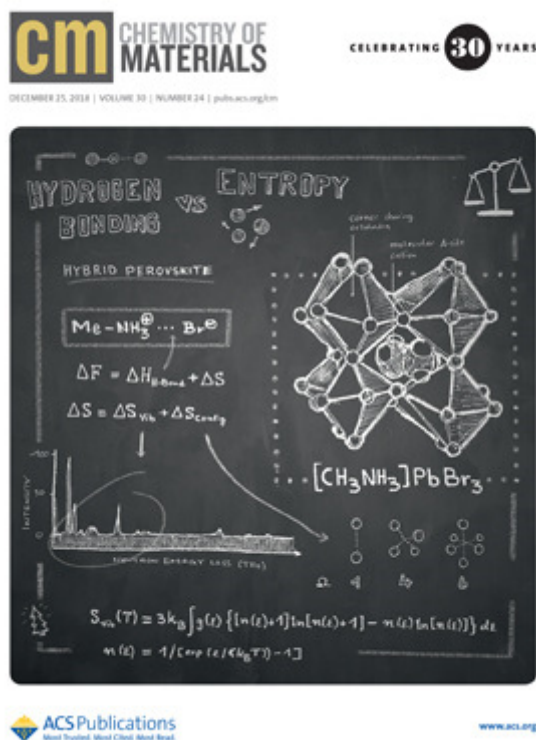
K. Butler, D. Bodeshiem

Figure 6: Cover of Chemistry of Materials, December 26, 2018

Volume 30, Issue 24

By combining inelastic neutron scattering with high-performance computing in a collaboration between SCD, ISIS Neutron and Muon Source, Technical University of Munich Nankai University we have been able to understand how structure evolves in hybrid organic-inorganic materials (HOIMs).

HOIMs have recently risen to prominence as a new generation of champion photovoltaic materials, promising to revolutionise solar power, they are also expected to have application in fields such as catalysis and solid-state cooling. These materials display a fascinating array of chemical and physical properties, not least of which is the ability to change structure in response to a variety of external stimuli (e.g. light, pressure, temperature). We have used the unique properties of neutrons along with quantum mechanical calculations to understand these phase evolutions and in the process have uncovered a new class of phase transition driven by the vibrations of these hybrid materials.

The 'vibrational entropy driven phase transition' mechanism turns out to be important in these hybrid materials. A delicate balance between weak interactions (such as hydrogen bonds) and disorder- or entropy-driven stabilisation means that researchers can have exquisite control of the response properties of the materials. The discovery and understanding of this mechanism opens up a new design paradigm for responsive HOIMs.

The work was only possible due to the combination of neutron scattering and high-performance computing. Neutrons measured the vibrational spectrum of the materials while

HPC allowed us to perform the 'lattice dynamics' calculations that shed light on the atomic scale vibrations that give rise to the spectrum.

The work was featured on the cover of Chemistry of Materials and appeared in a number of other high-impact publications.

Adsorption of formic acid on Fe₃O₄(001) and exploiting convolution neural networks to rapidly fit X-ray photoelectron spectroscopy data

D. A. Duncan

Diamond Light Source

Energy scanned photoelectron diffraction (PhD) is a unique technique that provides chemically specific, highly local structural information with a resolution down to hundredths of an Ångstrom. As electrons are interact strongly with matter, they can elastically scatter multiple times before being scattered towards our detector, thus there are no direct methods for PhD analyses, instead we must perform multiple scattering calculations, comparing theoretically calculated PhD modulations for a given model with those measured experimentally. In 2019 my student (Paul Ryan) has utilised the SCARF cluster to analyse PhD data of Formic acid on the surface of magnetite, determining the that O atoms of formic acid adsorb, dissociating one hydrogen atom that then binds to a surface oxygen atom (OH), as shown in Fig. 6.
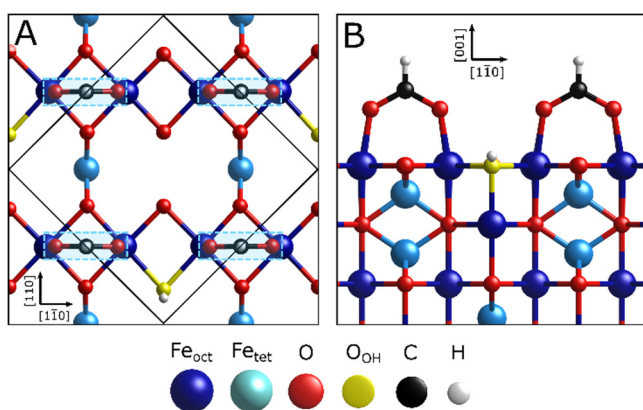
Figure 7: Schematic of the determined adsorption site of formic acid adsorbed on Fe3O4(001) shown in A) a plan view and B) a side view. Note that upon adsorption the H atom bound to one of formic acid's O atoms dissociates and binds to a surface oxygen atom, who site has also been determined by this method.

X-ray photoelectron Spectroscopy (XPS) is one of the most commonly used techniques in surface science, and is exploited in several other more advanced techniques (e.g. PhD or X-ray standing waves). Often, in order to gain relevant information from XPS it is necessary to fit the spectra with Gaussian like lineshapes. Such work is relatively straightforward for a human to perform, however on the beam line we can easily acquire several hundred XP spectra in a given day and many spectra go unanalysed in this manner because of this fact. Thus, an automated, on the fly analyses for XPS would be desireable for the various beam lines that utilise this technique. My student, in 2019 (Peter Starrs), developed a convolutional neural network that could be used to identify the number of peaks in an experimental spectrum and then suggest reasonable positions for those peaks, information that could then be used as inputs for a standard least-squares gradient descent optimisation as shown in Fig. 2.
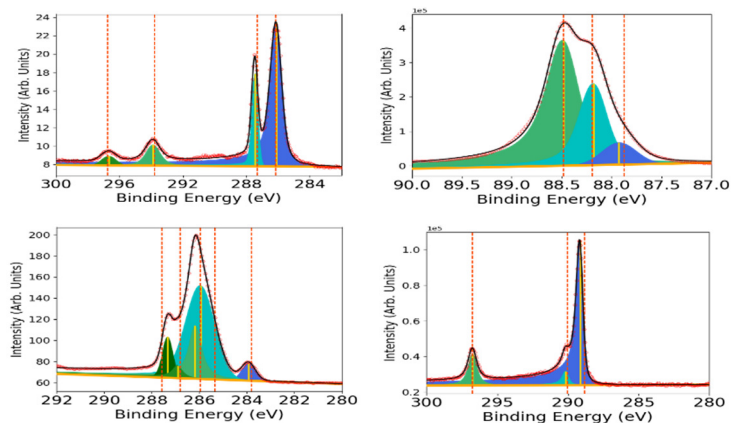
Figure 8: Fits to experimental data exploiting the convolution neural network for predicting the number and position of peaks. The red circles are the raw experimental data, the solid black line the sum of the fitted peaks, the solid coloured shapes the individual fitted peaks and the dashed orange lines indicate the predicted position.

Quantum motion of muons and muon spin relaxation (μSR)

Matjaž Gomilšek[1,2], Tom Lancaster[2], Stewart J. Clark[2], Francis L. Pratt[3] and Stephen P. Cottrell[3]

1. *Jožef Stefan Institute, Jamova c. 39, SI-1000 Ljubljana, Slovenia*
2. *Centre for Materials Physics, Durham University, South Road, Durham, DH1 3LE, UK*
3. *ISIS Facility, Rutherford Appleton Laboratory, Chilton, Didcot OX11 0QX, UK*

In muon spin rotation and relaxation (μSR) we implant short-lived muons μ+ in a material and measure their spin precession due to local magnetic fields present in the material at their stopping site. This powerful experimental technique is sensitive to a wide range of local magnetic fields (~0.1 mT to a few T) in a unique frequency window (0 Hz and ~10 kHz to ~1 THz) without the need for an applied field.

A drawback of μSR is that the μ+ stopping site in a material is *a priori* unknown, as is the magnitude of any muon-induced local structural distortions. This issue has recently been tackled via *ab initio* density functional theory (DFT) calculations of μ+ stopping sites [Fig. 8(b)], with mostly satisfactory results [1]. These, however, assume μ+ is a classical point particle at rest, which is often not a valid approximation.

As muons are ~9-times lighter than hydrogen they should substantially delocalize around their classical stopping sites due to quantum zero-point motion in their local (usually shallow) potential minimum and should have significant site-dependent quantum zero-point energy (~0.5 eV). Experiments even suggest that μ+ can undergo quantum tunnelling between different stopping sites and form coherent Bloch waves [2]. Describing these quantum effects of muon motion requires extending the standard *ab initio* methodology to fully encompass the quantum nature of μ+ and of the surrounding nuclei.

We tackle the problem of quantum muon motion via path-integral molecular-dynamics (PIMD) with the CASTEP DFT code [3]. These were carried out in part using SCARF computational facilities. In a case-study of μ+ in solid nitrogen α-N2 [Fig. 8(b,c)] [4] we demonstrate the necessity of properly accounting for the quantum motion of μ+ when interpreting experimental results and verify our predictions against experimental μSR results from ISIS, RAL, Didcot, UK.
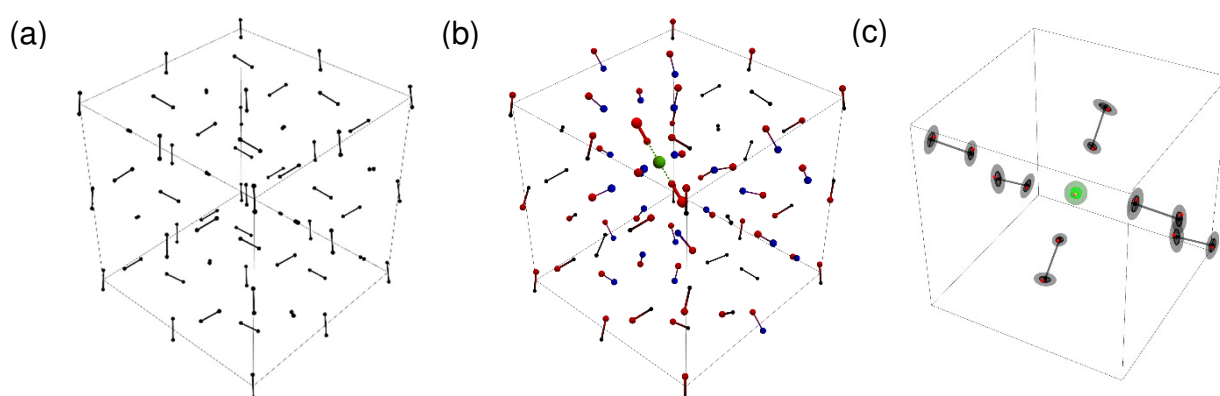
Figure 9: Pristine structure of solid nitrogen α-N2. (b) α-N2 with an implanted μ+ forming an N2–μ+–N2 covalent complex. The colours and sizes of atoms indicate their electric charge (red for positive, blue for negative, green for the muon). (c) Quantum zero-point motion of μ+ in α-N2 (green) and the quantum-entangled motion of nearby nitrogen atoms (grey).

References:

[1] J. S. Möller *et al.*, Phys. Scr. **88**, 068510 (2013).
[2] V. G. Storchak and N. V. Prokof'ev, Rev. Mod. Phys. **70**, 929 (1998).
[3] S. J. Clark *et al.*, Z. Kristallogr. Cryst. Mater 220, 567 (2005).
[4] M. Gomilšek *et al.*, in preparation.

Ab initio determination of spin-model parameters

Matjaž Gomilšek[1,2], Tina Arh[1], Peter Prelovšek[1], Matej Pregelj[1], Martin Klanjšek[1], Andrzej Ozarowski[3], Stewart J. Clark[2], Tom Lancaster[2], Wei Sun[4], Jin-Xiao Mi[4] and Andrej Zorko[1,5]

1. *Jožef Stefan Institute, Jamova c. 39, SI-1000 Ljubljana, Slovenia*
2. *Centre for Materials Physics, Durham University, South Road, Durham, DH1 3LE, UK*
3. *National High Magnetic Field Laboratory, Florida State University, Tallahassee, Florida 32310, USA*
4. *Fujian Provincial Key Laboratory of Advanced Materials, Department of Materials Science and Engineering, College of Materials, Xiamen University, Xiamen 361005, Fujian Province, People's Republic of China*
5. *Faculty of Mathematics and Physics, University of Ljubljana, Jadranska u. 19, SI-1000 Ljubljana, Slovenia*

A common problem in magnetism is the determination of relevant microscopic spin-model exchange parameters, which give rise to a material's magnetic behaviour. Complementary to experimental measurements, whose interpretation depends on an assumed spin model, various *ab initio* calculation schemes have been developed to directly derive a full spin model from a material's crystal structure [1]. Amongst the most widely used approaches is the broken-symmetry (BS, total-energy) method based on density functional theory (DFT) calculations.

We have performed large-scale BS DFT calculations at the LDA+U level to derive a spin model for $YCu_3(OH)_6Cl_3$ [2], a new and rare realization of a defect- and distortion-free quantum kagome antiferromagnet (KAFM) [3,4]. Unlike the ideal nearest-neighbour Heisenberg KAFM, which has a disordered quantum-spin-liquid (QSL) ground state, $YCu_3(OH)_6Cl_3$ magnetically orders at low T. BS DFT calculations, performed in part using SCARF computational facilities with the CASTEP DFT code [5], in combination with experimental results (Fig. 10) [2] have enabled us to determine that the origin of magnetic order in $YCu_3(OH)_6Cl_3$ is strong Dzyaloshinskii-Moriya magnetic anisotropy that pushes it the quantum critical point separating a QSL from a magnetically-ordered KAFM ground state.
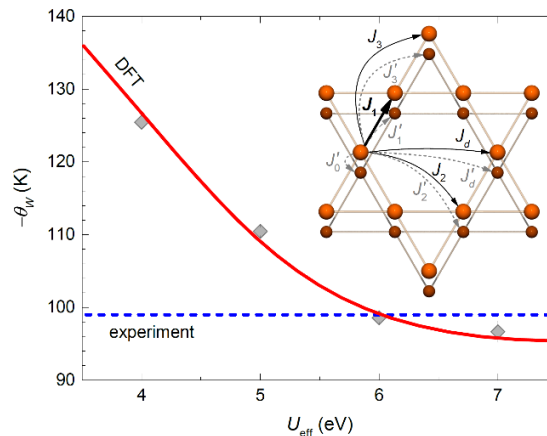
Figure 10: Dependence of the BS DFT+U calculated Weiss temperature (red) on the Hubbard U compared with experiment (blue) for the kagome antiferromagnet YCu3(OH)6Cl3. Inset shows its crystal structure and spin model. Reproduced from [2].

References:

[1] K. Riedl *et al.*, Phys. Status Solidi B **256**, 1800684 (2019).
[2] T. Arh *et al.*, arXiv:1912.09047. Submitted for publication.
[3] A. Zorko *et al.*, Phys. Rev. B **99**, 214441 (2019).
[4] A. Zorko *et al.*, Phys. Rev. B **100**, 144420 (2019).
[5] S. J. Clark *et al.*, Z. Kristallogr. Cryst. Mater 220, 567 (2005).

## Computational Analysis of the LiNH$_2$-Li$_2$NH Solid Solution

E. Chadwick, L. Liborio, S. Sturniolo

Theoretical and Computational Physics Group, Scientific Computing Department, RAL, STFC-UKRI, UK

The significant potential of hydrogen as a sustainable fuel can only be fulfilled if it is stored in a dense form [1]. Chemical methods avoid the need for extreme pressures or temperatures by reversibly bonding hydrogen to other elements. Liquid ammonia (NH$_3$) and solid materials such as lithium amides and imides have been considered for this purpose.

Lithium amide (LiNH$_2$) can be thermally decomposed to form lithium imide (Li$_2$NH). This process involves the synthesis of an intermediate lithium amide-imide solid solution, which can both allow the chemical storage of hydrogen and act as an ammonia decomposition catalyst [2]. There are several experimental studies on the properties of this solid solution [3, 4], but its atomic structure remains unknown. A recent paper by Makepeace and David [2] proposes using Raman spectroscopy to study the proportion of amide-imide groups present. The work presented here uses computational modelling to complement experimental studies on the lithium amide-imide solid solution, with a focus on understanding its structure.

Possible structures of the lithium amide-imide solid solutions were modelled by progressively removing H atoms from the lithium amide cell and adding Li atoms, to produce cells with stoichiometries given by Li$_{1+x}$NH$_{2-x}$, with $0 < x < 0.875$. First principles calculations were performed with CASTEP [5] on the different defect configurations available for each value of x. The lowest-energy configuration for each x was chosen as representative of that particular stoichiometry. In general, we find that the lowest-energy configuration for each x value has all the defects close together: new Li atoms are placed at adjacent cubic sites, and H atoms are removed from sites close to those new Li atoms. Figure 11 shows some of these configurations.

x=0   x=0.5   x=0.875
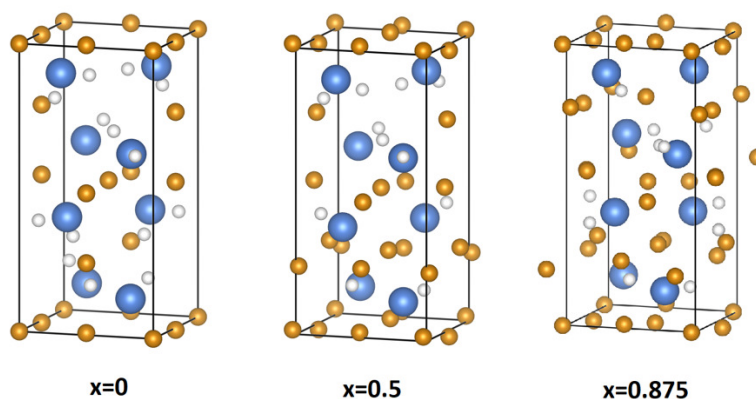
Figure 11: Example of configurations for Li1+xNH2–x

Figure 12 compares our simulation results (colour) with experimental data (black) from Makepeace and David [2] for Raman spectroscopy results. There is currently no experimental data for x = 0.125 and x = 0.875. We observe three types of stretch: symmetric NH2 stretches (S), asymmetric NH2 stretches (A) and N-H 'imide' stretches (I). The number of I peaks increases with x, and these are concentrated at lower frequencies, as the solid solution's stoichiometry moves towards being 'imide-like'. On the other hand, S and A peaks decrease in number, but these are often grouped around the same frequencies – this is because the defects created in the solid solution are grouped together, so some regions of the solid solution remain 'amide-like' and produce peaks matching amide frequencies. Some lower- frequency S and A peaks arise from NH$_2$ groups that are surrounded by a mix of NH and NH$_2$ groups.

Overall, we see agreement between the experimental broadening of the peaks and the behaviour of the simulated peaks. Our results support the hypothesis that NH and NH2 groups produce different Raman signals depending on whether they are in an amide-like, imide-like or non-stoichiometric local environment.
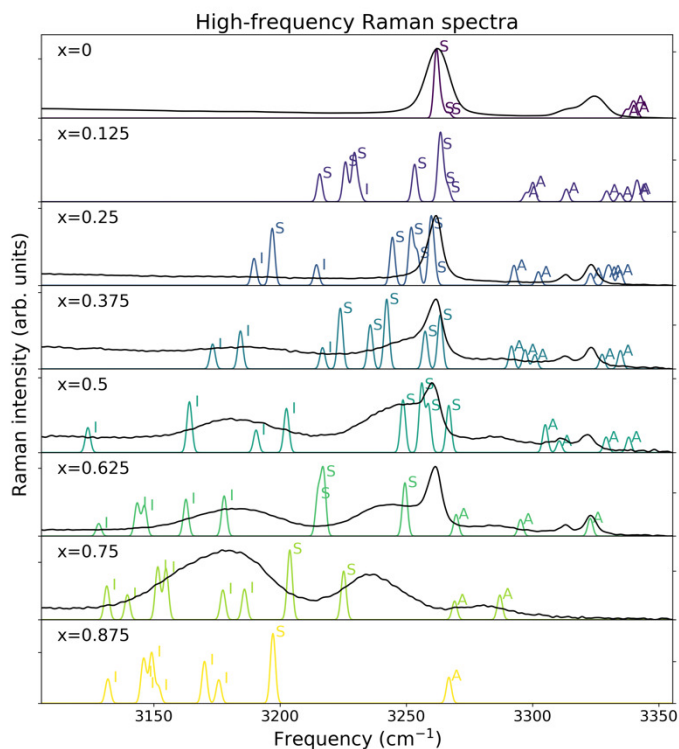
Figure 12: Experimental and theoretical Raman spectroscopy

Our simulated Raman results show reasonable agreement with experimental data, and suggest that the behaviour of NH and NH_2 groups in the lithium amide-imide solid solution changes depending on their local environment. Further Raman studies of the solid solution will provide a deeper insight into the variations in behaviour of the amide and imide groups.

References:

[1] Energy Environ. Sci. 5 (4 2012).
[2] JPCC C 121.22 (2017).
[3] Chem. Sci. 6 (7 2015).
[4] JACS 129.6 (2007).
[5] Zeitschrift fu¨r Kristallographie 220 (2005)

Ion acceleration by hole boring in solid hydrogen enhanced by relativistic self-focusing and channelling

Philip Martin, Satyabrata Kar, and Marco Borghesi

Centre for Plasma Physics, School of Mathematics and Physics, Queen's University Belfast, Belfast BT7 1NN, United Kingdom

The use of solid hydrogen as a target has piqued interest in recent times [1-3] not just for its delivery of a proton beam free from heavy ion impurities. The lower density of solid hydrogen, roughly an order of magnitude lower than plastic, means that ion acceleration by radiation pressure can be enhanced, specifically in the hole boring regime, which states that the maximum energies achieved by ions by this method is given by the relation [4]:

$$E_{max} \propto \frac{2\Pi}{1 + 2\sqrt{\Pi}} \qquad \Pi \equiv \frac{I_0}{\rho c^3}$$

Where I_0 is the peak laser intensity, ρ is the target density, and c is the speed of light in vacuum. Simulations were carried out on the particle-in-cell code EPOCH in 2D, where a Gaussian laser pulse with wavelength 1054nm, pulse duration (FWHM) of 750fs, and peak intensity of 5×10^{20} W/cm^2 was focused at an angle of 20 degrees to a 6µm wide (FWHM) spot. The target was a 20µm thick slab composed of solid hydrogen at a density of 54n_c, where n_c is the critical density for the laser. A significant self-focusing effect is observed (Fig. 13), where the pulse focuses down to a width roughly equal the laser wavelength. The intensity correspondingly increases to 2×10^{21} W/cm^2, enhancing the energies of protons accelerated from the front surface by hole boring. Fig. 14 shows the maximum hole boring proton energy measured for simulations at various input intensities ($a_0 \propto \sqrt{I\lambda^2}$).
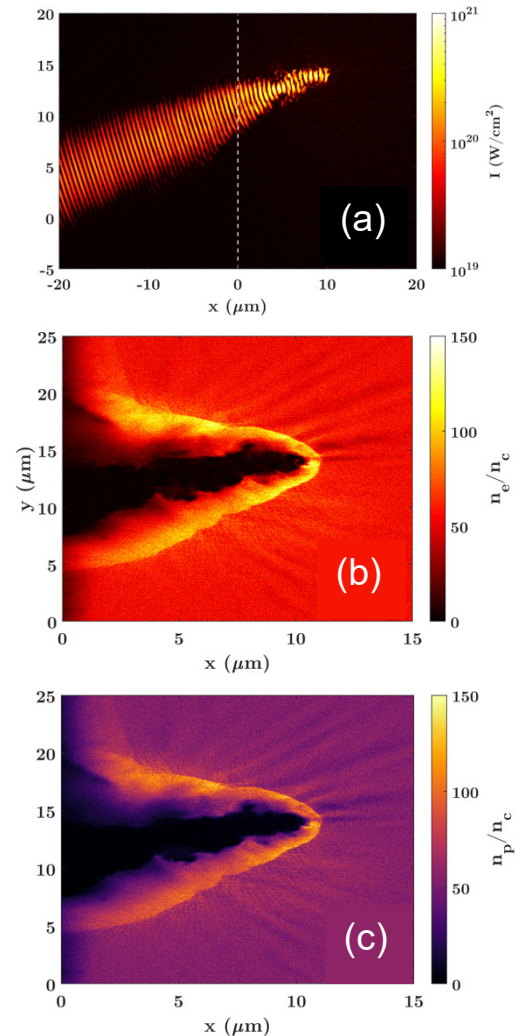
Figure 13: (a) Channelling and self-focusing of the laser pulse. The front of the target is denoted by the dashed line. (b) Electron, and (c) proton densities in the region of the channel.
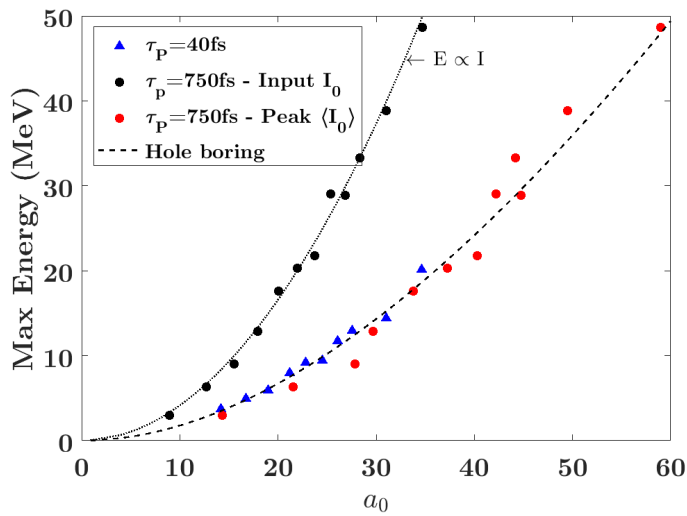
Figure 14: Max proton energies from hole boring, for various input intensities (black circles). The red circles are the same data points, plotted with the measured peak intensity after self-focusing, which follows the hole boring energies predicted analytically. Blue data points are for a shorter pulse, which experiences no self-focusing, also following the analytically predicted curve.

References:

[1] "Proton Acceleration Driven by a Nanosecond Laser from a Cryogenic Thin Solid-Hydrogen Ribbon", D. Margarone, A. Velyhan, J. Dostal, J. Ullschmied, J. P. Perin, D. Chatain, S. Garcia, P. Bonnay, T. Pisarczyk, R. Dudzak, M. Rosinski, J. Krasa, L. Giuffrida, J. Prokupek, V. Scuderi, J. Psikal, M. Kucharik, M. De Marco, J. Cikhardt, E. Krousky, Z. Kali- nowska, T. Chodukowski, G. A P Cirrone, and G. Korn. Phys. Rev. X 6 4 (2016)

[2] "First demonstration of multi-MeV proton acceleration from a cryogenic hydrogen ribbon target" S. D Kraft, L. Obst, J. Metzkes-Ng, H.-P. Schlenvoigt, K. Zeil, S. Michaux, D. Chatain, J.-P. Perin, S. N. Chen, J. Fuchs, M. Gauthier, T. E. Cowan, and U. Schramm. Plasma Phys. Control. Fusion, 60 044010 (2018)

[3] "Efficient Laser-Driven Proton Acceleration from a Cryogenic Solid Hydrogen Target", J. Polz, A. P. L. Robinson, A. Kalinin, G.A. Becker, R.A. Costa Fraga, M. Hellwing, M. Hornung, S. Keppler, A. Kessler, D. Klöpfel, H. Liebetrau, F. Schorcht, J. Hein1, M. Zepf, R. E.Grisenti, M. C. Kaluza, Sci. Reports 9 16534 (2019)

[4] "Relativistically correct hole-boring and ion acceleration by circularly polarized laser pulses", A. P. L. Robinson, P. Gibbon, M. Zepf, S. Kar, R. G. Evans and C. Bellei, Plasma Phys. Contol. Fusion 51 024004 (2009)

Modelling the Water and (bio)materials Interface: Combining Neutron Scattering and in-silico studies

Jose A Martinez-Gonzalez[1], Ilian Todorov[2] and Victoria Garcia Sakai[1]

1. *ISIS Neutron and Muon Source, STFC Rutherford Appleton Laboratory, Harwell Oxford, Didcot.*
2. *Computational Chemistry Group, STFC Daresbury Laboratory, Sci-Tech Daresbury, Keckwick Lane, Daresbury.*

Understanding the interactions between water and the surface of biomaterials is fundamental, for understanding wettability phenomena, adhesion of proteins or tissue regeneration around implant. Water in contact with the surface, so-called interfacial water, has attracted plenty of interest for many years. The properties of interfacial water are dependent on the specific interactions with the biomaterial, and typically result in significant changes to bulk state, such as the prevention of ice formation, water remaining in a glassy state below the freezing point of water. This project wants to improve the knowledge of the properties of this interfacial water using a combination of experimental and theoretical approaches.

We are using DL_Software package, developed by Computational Chemistry group at SCD, and Gromacs Software to obtain different classical molecular dynamics (MD) simulation of several materials, such as silicon, zeolites or phospholipids membrane in contact with water. At this stage, we perform several MD simulations and we are analysing the results via MDanse software to obtain the quasi-elactic neutron scattering profiles in order to compare with the experiments that we are perform at ISIS facilities and also with other previous research. A visual representations of the interfacial water in contact with different materials and a comparative between experimental and simulated results are shown at Figure 15.
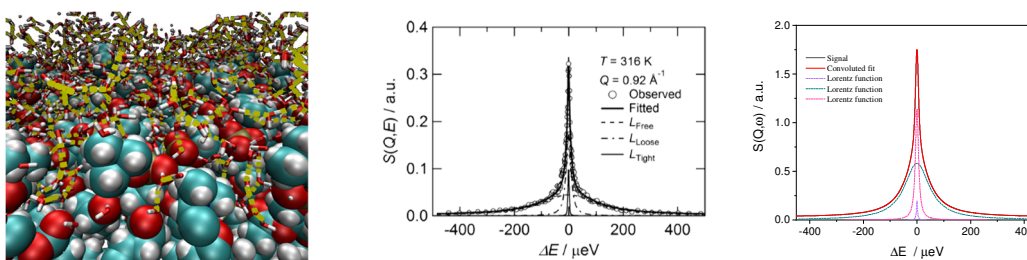
Figure 15: Visual representation of the interfacial water in contact with POPC (left) and QENS experimental (centre) and simulated profile (right)

Vibrational Dynamics Of Benzaldehyde Derivatives From Periodic DFT Calculations

Mariela M. Nolasco,[1] Catarina F. Araujo,[1] Paulo J. A. Ribeiro-Claro,[1] Pedro D. Vaz,[2] and Ana M. Amado[3]

1. *CICECO – Aveiro Institute of Materials, Departamento de Química, Universidade de Aveiro, 3810-193 Aveiro, Portugal*
2. *Champalimaud Foundation, Champalimaud Centre for the Unknown, 1400-038 Lisboa, Portugal*
3. *Química-Física Molecular, Departamento de Química, FCTUC, Universidade de Coimbra, P-3004-535 Coimbra, Portugal*

At present, there is a limited number of reports addressing the vibrational spectra of molecular crystals using periodic density functional (DFT) calculations. However, although originally developed to deal with inorganic systems it becomes evident that the periodic DFT approach, is able to predict the vibrational spectra of molecular crystals with very good accuracy. In particular, the CASTEP code is becoming increasingly popular to assess the infrared and, more interestingly, the inelastic neutron scattering (INS) spectra of molecular crystals. Raman intensities are also available, but are seldom reported due the inherent large computational cost.

The comparison between the calculated and experimental inelastic neutron scattering (INS) spectra is crucial, as INS provides information not easily amenable from optical techniques. In INS, the signal intensity is highly dependent on the motions of hydrogen atoms and, due to the absence of selection rules, all vibrational modes are permitted. In this way, low wavenumber / large amplitude vibrational motions are readily observed in INS spectra.
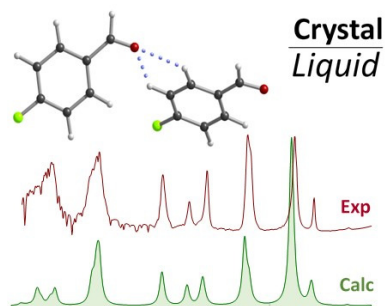
This project aims to assess the vibrational dynamics of crystalline benzaldehyde derivatives through the analysis of INS and IR spectra. To this end, a detailed description of the vibrational modes is obtained from periodic DFT calculations.

Figure 16 compares the experimental and calculated INS spectra of 4-phenylbenzaldehyde. The nearly one-to-one correspondence between observed and calculated bands provides a detailed assignment of the INS spectrum.

Figure 16: Comparison of the experimental and calculated INS spectra of 4-phenylbenzaldehyde

In the case of 4-fluorobenzaldehyde, the absence of a reported crystalline structure was superseded by using a starting crystalline structure derived from the one reported for 4-chlorobenzaldehyde, which is structurally similar to its parent compound 4-bromobenzaldehyde, lending credence to the hypothesis that 4-fluorobenzaldehyde is isomorphous with its chloro- and bromo- analogues. Geometry optimization was then performed with fixed cell parameters. Figure 17 illustrates the excellent fit between calculated and experimental spectra obtained from this approach. Additionally, the feasibility of using periodic DFT calculations to assist the interpretation of vibrational spectra of liquids and non-crystalline solids is discussed.

Figure 17: Illustration of the fit between calculated and experimental spectra

These results are presented in greater detail in a recent publication [1] and further works are expected to be published in the near future.

References:

[1] P. Ribeiro-Claro, P. D. Vaz, M. M. Nolasco, C. F. Araujo, F. P. S. C. Gil, A. M. Amado, *Vibrational dynamics of 4-fluorobenzaldehyde from periodic DFT calculations,* Chem. Phys. Lett. X, **2** (2019) 100006. DOI: 10.1016/j.cpletx.2019.10000

Exploring Asymmetry-Induced Entropy In Deep Eutectic Solvents

Catarina F. Araujo[1], João A. P. Coutinho[1], Paulo J. A. Ribeiro-Claro[1], Svemir Rudić[2], Pedro D. Vaz[3] and Mariela M. Nolasco[1]

1. *CICECO – Aveiro Institute of Materials, Departamento de Química, Universidade de Aveiro, 3810-193 Aveiro, Portugal*
2. *ISIS Neutron & Muon Source, STFC Rutherford Appleton Laboratory, Chilton, Didcot, UK*
3. *Champalimaud Foundation, Champalimaud Centre for the Unknown, 1400-038 Lisboa, Portugal*

Deep eutectic solvents (DES) are a novel class of designer solvents hailed as the sustainable alternative to ionic liquids. The most common type of DES are formed by mixing a salt, usually a quaternary ammonium halide, with an hydrogen bond donor, including amides, amines, alcohols and carboxylic acids. The term "deep eutectic" arises from an interesting phenomenon: the melting point of a deep eutectic mixture is significantly lower than that of an ideal mixture of its components. For instance, the iconic DES named "Reline" consists of a mixture of choline chloride (ChCl) and urea, whose ideal mixture would melt at 75ºC while the real mixture (1 ChCl: 2 urea) melts close to 20ºC. The difference between the ideal and real melting temperature is often called "melting point depression" and the mechanism behind this phenomenon is still poorly understood, although it is apparent that both enthalpic and entropic factors are involved.
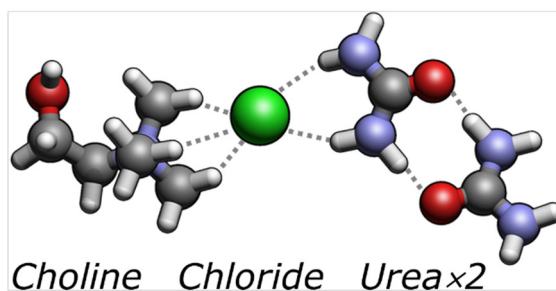

Figure 18: Deep eutectic solvents (DES) "Reline"

The most often cited rationalization for this phenomenon is that the hydrogen bond donor (HBD) interacts with the anion thus disrupting the salt's lattice, leading to charge delocalization and preventing crystallization, a result of entropic and enthalpic effects which are often difficult to tell apart. The influence of entropic changes remains unclear. It is well-known that salts with symmetric cations do not tend to form low melting mixtures, perhaps due to their greater ease of packing efficiently with the HBD, leading to ordered solids. However, most fundamental studies focused on enthalpic rather than entropic effects, a knowledge gap which this study aims to address by comparing systems with similar enthalpic profiles but contrasting degrees of cationic symmetry. For example, the (1:2) mixture of tetraethylammonium bromide and urea melts at 113ºC . Slightly tweak the cation – substituting an ethyl by a methyl group – and even though the hydrogen bonding capability has not been altered, the asymmetric cation leads to a mixture that melts at 9ºC. In this case, it is likely that the melting point depression is largely driven by entropic, rather than enthalpic factors, a matter which may be clarified through the use of Inelastic Neutron Scattering (INS).
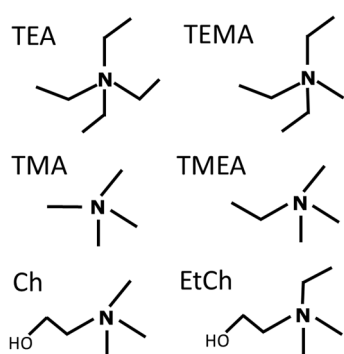
Figure 19

The INS spectra of several DES systems have been recorded on TOSCA. Vibrational assignments were guided by periodic CASTEP calculations performed on the SCARF cluster for the crystal structures of the pure components.

Advanced neutron tracking for the upgraded TS1-TRAM at ISIS: a roadmap toward the enhancement of the signal to noise ratio at the instrument sample location.

Lina Quintieri

ISIS Facility, STFC Rutherford Appleton Laboratory, Chilton, Didcot, OX11 0QX, UK

A detailed and highly accurate model of the new TS1 TRAM has been built with the FLUKA code, aimed at providing both scientific and engineering relevant information, such as: neutron and other secondary particles yield, energy deposition profile, particle fluence energy spectrum, decay heat, overall radionuclide inventory etc. Exploiting an advanced usage of FLUKA, it has been possible to track the TRAM escaping neutrons in such a way to assess quantitatively the contribution of each target plate to the overall neutron leakage as well as the effective contribution of the water and cryogenic moderators to all the ISIS-TS1 instrument beam lines. The information about the origin (specific spatial region and material inside the TRAM) of the channelled neutrons in each beam-line could help to have a better understanding of the efficiency of the moderator and reflector assembly in terms of both the flux of neutrons delivered to the instruments and shape of the neutron energy spectrum at the instruments. A detailed record of relevant information of the previous history inside the TRAM is stored for (and assigned to) each tracked neutron transmitted in the instrument beamlines (i.e., if the channelled neutrons have effectively passed across moderators, which moderators have been actually visited, the last TRAM region they went through, their age at the sample respect to the primary proton pulse trigger time, etc). Technically, this is possible by exploiting advanced FLUKA scoring features, as the "*LATCHING*" and "*FLAGGING*" techniques, respectively. A first analysis to reconstruct the history of the neutrons arriving and channelling in the instrument beam lines has been already accomplished for several TS1 instruments: the results obtained for the Polaris Instrument are shortly reported hereafter, as an explicative (even if not fully exhaustive) example.

Neutrons at the Polaris inlet port:

- 0.04% is the fraction of the TRAM escaping neutrons actually impinging on the Polaris inlet window;

- Among those neutrons: 36.6% are below 1 keV; 63.4% above 1keV;

- 16.25% of all the impinging neutrons on Polaris are flagged 131, that is they have been actually in the moderator designed to feed the instrument itself.

Transmitted neutrons in Polaris:

- 340 cm far away from the inlet port, 82% of transmitted neutrons have actually been in the asymmetrically poisoned water moderator (flagged 131)

- The channelled neutrons have been generated mainly by direct spallation in the central target plates (no contribution from plates n.8, 9 and 10, these latter being the plates in the opposite location with respect to the proton impacted surface of the target);

- 72% of the channelled neutrons in Polaris have been produced in Tungsten. Anyway, a not negligible contribution comes from Beryllium and it is slightly higher than the contribution coming from Tantalum cladding
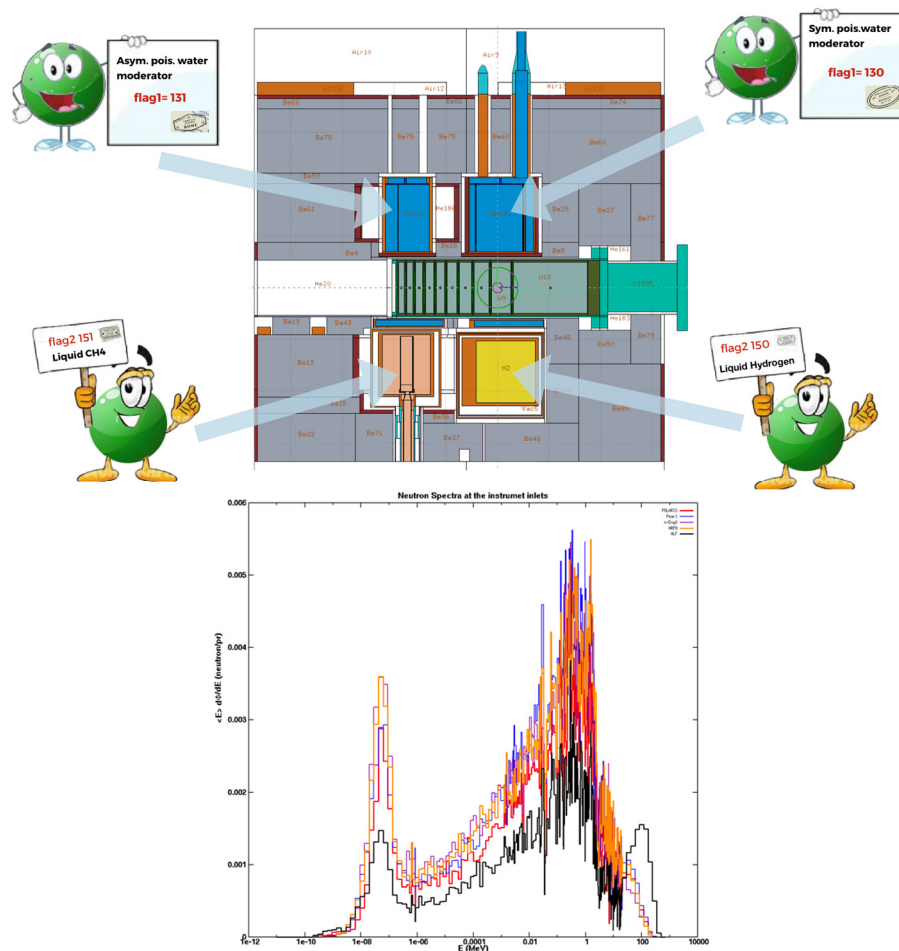
Figure 20: (Upper) Flagged neutron labels; (lower) Neutron energy spectra at several instruments' inlet ports

References:

[1] A. Fassò et al. - FLUKA: a multi-particle transport code, Tech. Rep. CERN- 2005-10 (2005), INFN/TC-05/11,SLAC-R-773

AEROBIC OXIDATION OF STYRENE BY IMMOBILIZED AU NANOPARTICLES IN CO/AL HYDROTALCITE – SHEDDING LIGHT ON THE MECHANISM

Sónia R. Leandro,[1] Cristina I. Fernandes,[1] Ana S. Viana,[1,2] Ana C. Mourato,[1] Pedro D. Vaz,[3] Carla D. Nunes[1,3*]

1. *Centro de Química e Bioquímica, Faculdade de Ciências da Universidade de Lisboa, 1749-016 Lisboa, Portugal*
2. *Centro de Química Estrutural, Faculdade de Ciências e Instituto Superior Técnico, Universidade de Lisboa, 1049-001 Lisboa, Portugal*
3. *CICECO – Aveiro Institute of Materials, Department of Chemistry, University of Aveiro, 3810-193 Aveiro, Portugal*

Current environmental concerns are focused on the development of cheap catalysts leading to highly selective materials and therefore reducing by-products. Such concerns aim at a lower consumption of natural resources as well as benign and impactless reaction media. A large fraction of catalytic processes makes use of precious metals (second- and third-row transition metals). While still much unrivaled in terms of catalytic performance, these metals suffer from many drawbacks impacting negatively both industry and society. On the other hand, Nature sustains its activity and offers an incredible range of materials relying on metals (Mg, Ca, Mn, Fe, Co, Ni, Cu, Zn, Al) that are typically cheaper, less toxic, and more benign than their heavier counterparts [4]. Exploring this rapidly, expanding new frontier in a field that is of importance for practical reasons (cost and availability, environmental impact, toxicity), will aim at the discovery of fundamentally new reactivity that can offer solutions to a broader range of catalytic problems. Understanding better the upgrading processes and developing viable alternatives will contribute to achieve new frontiers in catalysis.

Oxidation of styrene usually yields a set of economically valuable products: the epoxide, benzaldehyde and benzoic acid, according to the mechanistic proposal in the Figure 21.
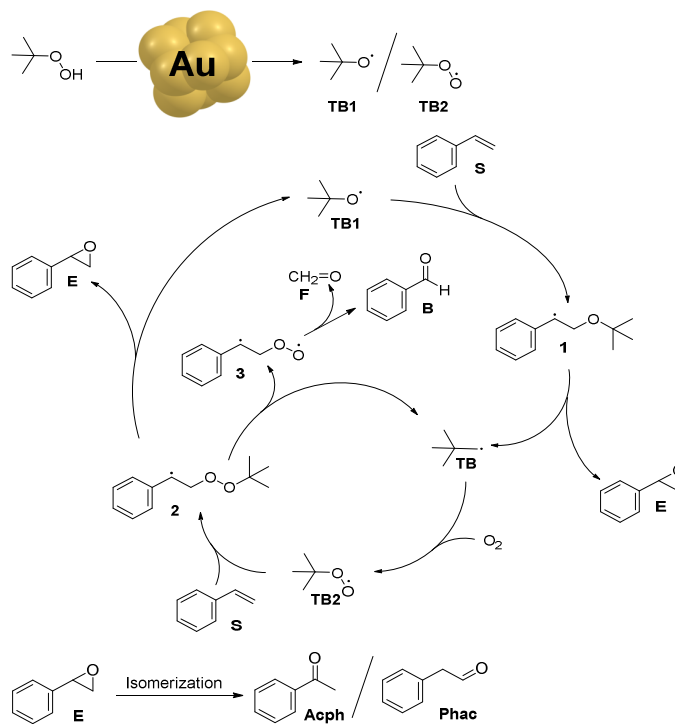
Figure 21: Oxidation of styrene

The above proposal demonstrates how the radical mechanism may progress as styrene lacks the presence of H-atoms in α-position to the olefin moiety, which would make impossible to rationalize H-atom abstraction [1]. Alternatively, styrene recombines directly with tbhp radicals yielding a couple of intermediaries (**1** and **2** in Figure 21). These will then decompose to yield either styrene oxide or benzaldehyde, depending on the path followed (Scheme 1). The *t*-butyl derivative radicals will recombine (or not) with O_2 closing and feeding the catalytic cycle [1].

In this work we present a study on this mechanistic proposal using Density Functional Theory (DFT) calculations by mean of the G09 package applied on the intermediaries mentioned above to assess the associated thermodynamics. All calculations were performed exclusively for the energetics of the reagents and products without accounting for the catalyst's influence.

The calculated energetics for the proposed mechanism confirmed that this proposal is realistic and viable, as found in Figure 22. From the results obtained it could be demonstrated the radical mechanism only needs the Au catalyst to form the initial **TB1**/**TB2** initiators. After that step, the reaction is self-fed by a cascade of steps terminating in the desired products – styrene oxide and benzaldehyde. Isomerization of the former may lead to formation of acetophenone or phenylacetaldehyde as by-products. DFT results showed that both by-products are feasible. The calculations also evidenced that the spin densities in the radical species are localized specifically in the oxygen atoms (when present) with the exception of intermediaries **1** and **2**, where the spin density is localized in the C atom, as expected, since this will subsequently originate a nucleophilic attack to yield the epoxide product.The mechanistic proposal for styrene oxidation based on DFT calculations, also revealed that the regeneration of the *tert*-butyl radical (**TB** yielding **TB2**) may be responsible for the rate determining step, in addition to formation of intermediaries **1** and **2** (Figure 21).

This renders excellent perspectives for future developments of this system, which are being further endeavoured by us. These results were reported in more detail in a recently published work [2].
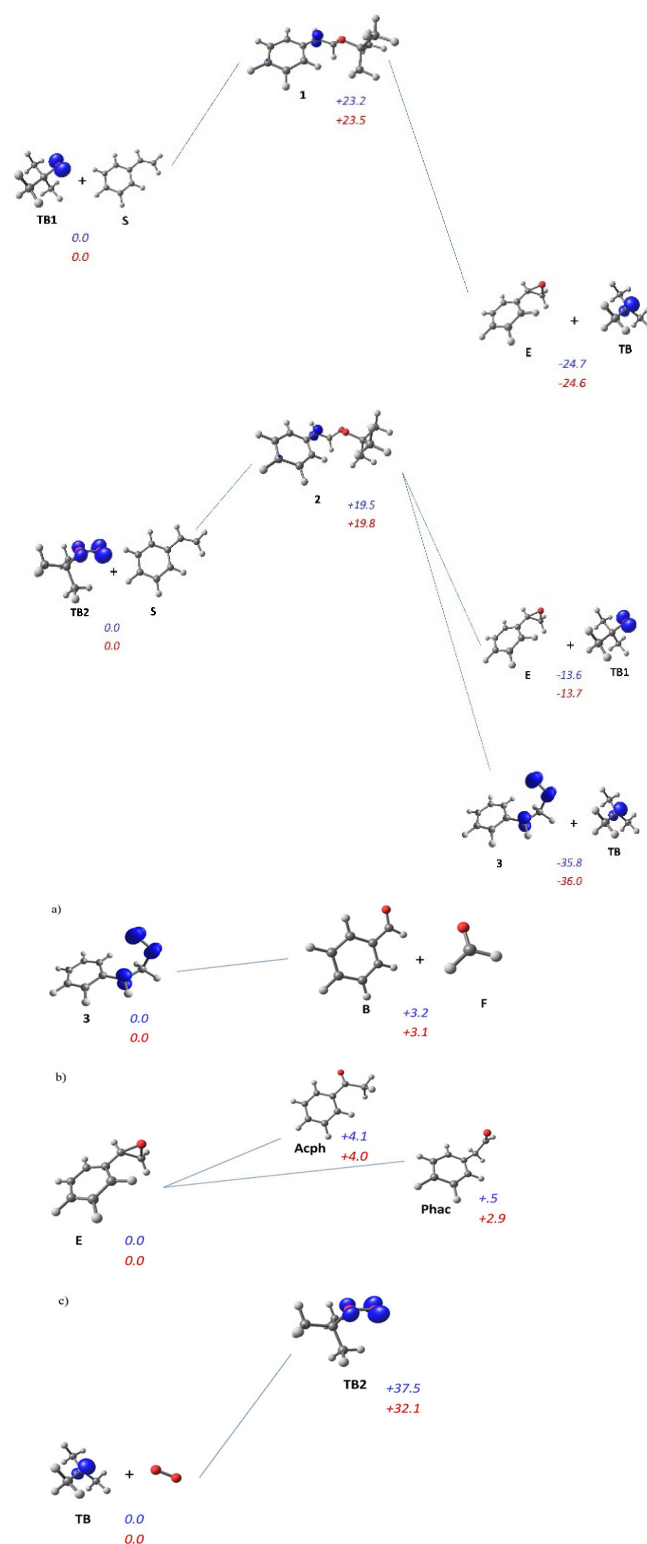
Figure 22: Free energy profile (kcal mol-1) for the mechanistic proposal (Figure 20). The top values correspond to those calculated in acetonitrile (blue) while the bottom ones were obtained for toluene (red) and are reported for the experimental reaction temperature (353 K). The spin density of the radicals was plotted in blue with a 0.05 cut-off.

References:
[1] S. R. Leandro, A. Mourato, U. Łapińska, O. C. Monteiro, C. I. Fernandes, C. D. Nunes, P. D. Vaz, *Exploring bulk and colloidal Mg/Al hydrotalcite-Au nanoparticles hybrid materials in aerobic olefin epoxidation*, J. Catal. **358** (2018) 187–198.
DOI: 10.1016/j.jcat.2017.12.014
[2] S. R. Leandro, C. I. Fernandes, A. S. Viana, A. C. Mourato, P. D. Vaz, C. D. Nunes, *Catalytic performance of bulk and colloidal Co/Al layered double hydroxide with Au nanoparticles in aerobic olefin oxidation*, Applied Catal. A: Gen., **584** (2019), 117155.
DOI: 10.1016/j.apcata.2019.117155

Unravelling Thermodynamic Secrets in 4'-Hydroxyacetophenone

Carlos E. S. Bernardes,[1,2] Manuel E. Minas da Piedade,[1,2] Victoria Garcia-Sakai,[3] Pedro D. Vaz[4,5]

1. *Centro de Química e Bioquímica, Faculdade de Ciências da Universidade de Lisboa, 1749-016 Lisboa, Portugal*
2. *Centro de Química Estrutural, Faculdade de Ciências e Instituto Superior Técnico, Universidade de Lisboa, 1049-001 Lisboa, Portugal*
3. *ISIS Neutron & Muon Source, STFC Rutherford Appleton Laboratory, Chilton, Didcot, Oxfordshire OX11 0QX, U.K.*
4. *CICECO – Aveiro Institute of Materials, Departamento de Química, Universidade de Aveiro, 3810-193 Aveiro, Portugal*
5. *Champalimaud Foundation, Champalimaud Centre for the Unknown, 1400-038 Lisboa, Portugal*

Polymorphism is a common phenomenon in molecular organic solids, which consists of the existence of more than one crystal form of the same compound. Polymorphs may differ not only in their packing architecture but also, sometimes, in the conformation of the molecules that define the crystal lattice. These differences are frequently large enough to affect the stability of a material regarding chemical reactivity, compression, solubility, and various other properties that need to be strictly controlled in industry sectors such as pharmaceuticals.

The industrial implications of polymorphism (e.g., lack of reproducible product manufacture, variations in shelf life, patenting of new forms) have fostered considerable efforts to devise strategies for the reproducible and selective preparation of crystal forms with the best properties for specific applications and manufacturing processes using crystal engineering strategies. This also raised some major challenges in terms of fundamental research, such as uncovering the structure–energetics features behind the relative stability of polymorphs and understanding how polymorphs may interconvert through phase transitions.

Efforts in these directions led about a decade ago to the proposal that polymorphs with $Z' > 1$ are metastable relative to their $Z' = 1$ analogues. The suggestion was born from the idea that from a crystallographic point of view clean-cut symmetry expression and stability should go hand in hand. High Z' structures might, therefore, correspond to arrested crystallization stages, originating by the nonequilibrium nature of the nucleation pathway, which would ultimately lead to a $Z' = 1$ form if thermodynamic control could be achieved. A significant number of exceptions showed, however, that a rationale centered on a structural conjecture alone cannot provide a universal

Figure 23: HAP forms I (top) and II (bottom).

measure of stability, as emphasized in a recent seminal review on high Z' crystal structures. Nevertheless, the fact that the exceptions are particularly common for certain types of compounds where there is difficulty in balancing close packing with hydrogen-bond (H-bond) formation also gives important clues on how specific types of intermolecular forces may favor a given molecular organization in the solid state.

Structure–stability discussions should not, however, be divorced from thermodynamics, which provides the appropriate theoretical framework to assess the relative stability of

molecular systems in general and, therefore, also of polymorphs. The investigation of enantiotropic systems involving two polymorphs with different Z' values is particularly interesting in the context of the structure–stability relationships mentioned above, since enantiotropy is characterized by the existence (at constant pressure) of a transition temperature before fusion at which the stability of the two forms is reversed.

4'-Hydroxyacetophenone (HAP) has proven to be a rich system in terms of solid form diversity, with at least two polymorphs and three hydrates identified and characterized from structural, solid state stability, and crystallization points of view. The anhydrous polymorphs also provide an opportunity to study structure–energetics relationships behind the adoption of high-Z' structures and their relative stability toward a $Z' = 1$ counterpart, when solid state conversion through a phase transition is a one way process due to kinetic hindrances. Indeed, DSC and X-ray diffraction (XRD) studies carried out at atmospheric pressure previously evidenced an irreversible phase transition between the two HAP polymorphs where packing, molecular conformation, and Z' simultaneously change. On heating HAP form II (orthorhombic, space group $P2_12_12_1$, $Z' = 2$) from ambient temperature, an endothermic transformation into form I (monoclinic, $P2_1/c$, $Z' = 1$) was observed at 351.2 ± 2.7 K.

The reverse process was not detected on cooling and both forms could be stored unaltered without strict control of laboratory temperature, pressure, or humidity. This robustness toward interconversion was observed, even if the available thermal energy at 298 K ($RT = 2.5$ kJ·mol^{-1}) was ~5 times larger than the difference between the lattice energies of forms II and I at that temperature (0.49 ± 0.13 kJ mol^{-1}) determined by solution calorimetry.

The reduction of the number of molecules in the asymmetric unit from $Z' = 2$ to $Z' = 1$ was accompanied by a change in molecular conformation, since the relative orientations of the OH and C=O groups switched from Z in form II to E in form I (Figure 23).

The Z conformations of the two molecules in the asymmetric unit of form II are very similar in terms of distances and dihedral angles. Moreover, although in both cases the 1D packing motifs consisted of infinite linear chains $C_1^1(8)$ sustained by "head-to-tail" bonding between the hydroxyl group of one molecule (donor) and the carbonyl group of an adjacent molecule (acceptor), the chains changed from helical in form II to linear in form I (Figure 23). It is finally worth mentioning that the higher lattice energy of the low temperature form II also corresponds to a slight density advantage, since the density of form II at 298 K (1.278 g·cm^{-3}) is 2.4% larger than that of form I (1.247 g·cm^{-3}), even though the packing fractions of both polymorphs are very similar (~0.70).
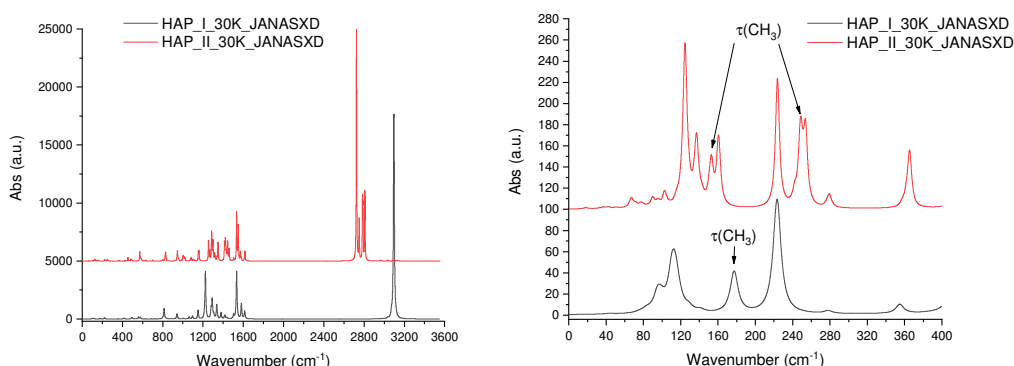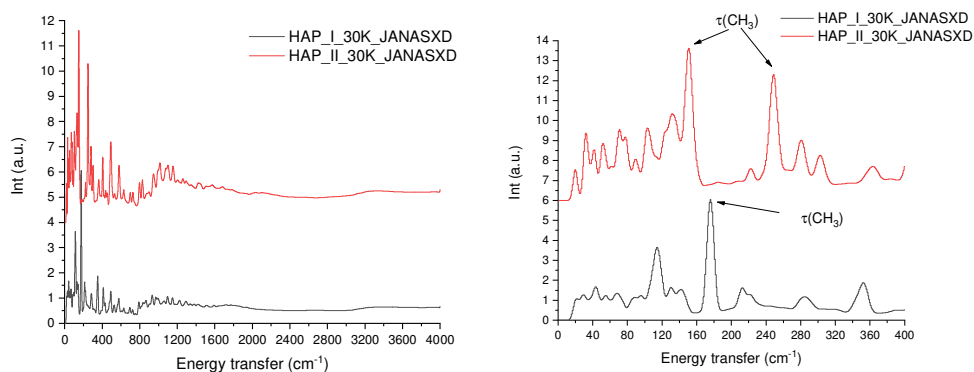
Figure 24: Far-IR (top) and INS (bottom) spectra of HAP forms I and II. It should be noticed, however, the clear advantage of INS due to the high intensity of low-frequency vibrations (below 800 cm-1) as compared to IR.

In this study we used CASTEP to simulate both the Infrared and the Inelastic Neutron Scattering (INS) spectra of both HAP forms and to assess eventual differences arising from the different packing motifs. This was done by performing a geometry optimization with fixed cell parameters for each form and then requesting calculation of the corresponding spectra. We found that the torsion modes of the methyl groups yield clear differences in the corresponding spectra and in agreement with their structures.

Figure 24 shows that for form I there is a single mode (agreeing with a single molecule in the asymmetric unit of the crystal, while in form II there are two modes expected, again agreeing with the fact that two molecules exist in the asymmetric unit. Further work is ongoing to correlate these findings with calorimetry, QENS and INS measurements.

References:

[1] C. E. S. Bernardes, M. F. M. Piedade, M. E. Minas da Piedade, *Polymorphism in 4'-Hydroxyacetophenone: Structure and Energetics*, Cryst. Growth Des. **2008**, 8, 2419– 2430. DOI: 10.1021/cg7012792

[2] A. Joseph, C. E. S. Bernardes, A. I. Druzhinina, R. M. Varushchenko, T. Y. Nguyen, F. Emmerling, L. Yuan, V. Dupray, G. Coquerel, M. E. Minas da Piedade, *Polymorphic Phase Transition in 4'-Hydroxyacetophenone: Equilibrium Temperature, Kinetic Barrier, and the Relative Stability of Z' = 1 and Z' = 2 Forms*, Cryst. Growth Des. **2017**, 8, 2419– 2430. DOI: 10.1021/acs.cgd.6b01876

The vibrational dynamics of chlorinated methane solvents – CH₂Cl₂, CHCl₃ and CCl₄.

Pedro D. Vaz,[1] Paulo J. A. Ribeiro-Claro,[2] Stewart F. Parker,[3] and Mariela M. Nolasco[2]

1. *Champalimaud Foundation, Champalimaud Centre for the Unknown, 1400-038 Lisboa, Portugal*
2. *CICECO – Aveiro Institute of Materials, Departamento de Química, Universidade de Aveiro, 3810-193 Aveiro, Portugal*
3. *ISIS Neutron & Muon Source, STFC Rutherford Appleton Laboratory, Chilton, Didcot, UK*

Chlorinated methane solvents are still much used as solvents for their convenience and advantages in chemical synthesis, catalysis or in spectroscopy, just to name a few applications. Their relevance is also of note due to the fact that all, except CCl_4, are capable of establishing H-bonds as donors [1].

In this study, we measured the Inelastic Neutron Scattering spectra of CH_2Cl_2, $CHCl_3$ and CCl_4 along with the infrared (IR) and Raman spectra. To understand the experimental results, we relied on the use of the CASTEP code to simulate the INS spectra and correlate this with the experimental data. The first step was to perform a geometry optimization with fixed cell parameters for each of the compounds and then requesting calculation of the corresponding spectra. Figure 25 illustrates the optimized geometries of the solvents under study.
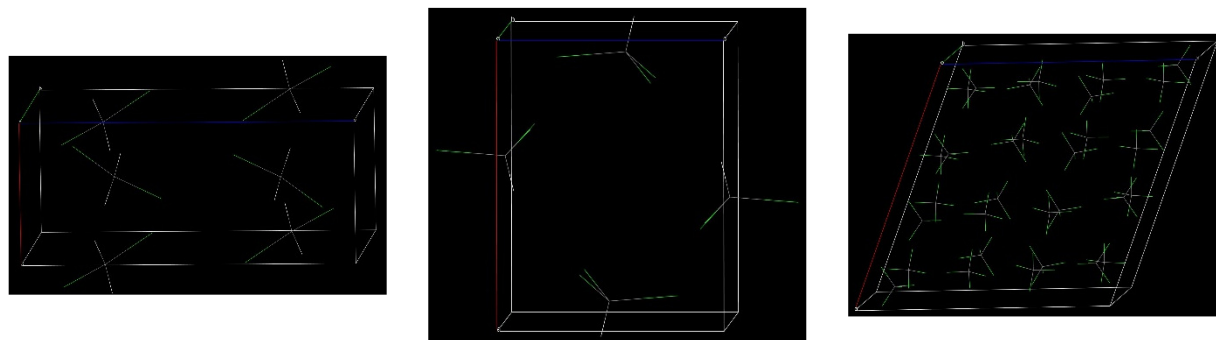
Figure 25: Optimized geometries with CASTEP of CH2Cl2, CHCl3 and CCl4.

This work is still at its first steps and further results are expected to be achieved during 2020.

References:
[1] Pedro D. Vaz, Mariela M. Nolasco, Francisco P. S. C. Gil, Paulo J. A. Ribeiro-Claro, John Tomkinson, *Hydrogen-Bond Dynamics of C–H···O Interactions: The Chloroform···Acetone Case*, Chem. Eur. J., **16** (2010), 9010 – 9017.

Electronic Excitations in Copper Oxides

A. Živković[1], B. Searle[2], L. Bernasconi[3]

1. *Cardiff University, School of Chemistry, Main Building Park Place, Cardiff CF10 3AT, United Kingdom.*
2. *STFC Daresbury Laboratory, Daresbury, Cheshire WA4 4AD, United Kingdom.*
3. *Center for Research Computing, University of Pittsburgh, 312 Schenley Place, 4420 Bayard Street, Pittsburgh, PA 15260, USA.*

Excitonic effects are amongst the key concepts that provide insight and understanding of electronic and optical properties of solids. Studying properties of solids under weak and strong photoexcitation is of fundamental importance to understand linear and nonlinear relaxation processes of excited states out of equilibrium [1]. Due to the increased interest in copper oxides for phovoltaic applications and as a promising *p*-type transparent conductive oxides, understanding of the exciton dynamics in these materials is of great importance as a vital basis to improve efficiencies in optoelectronic device applications [2].
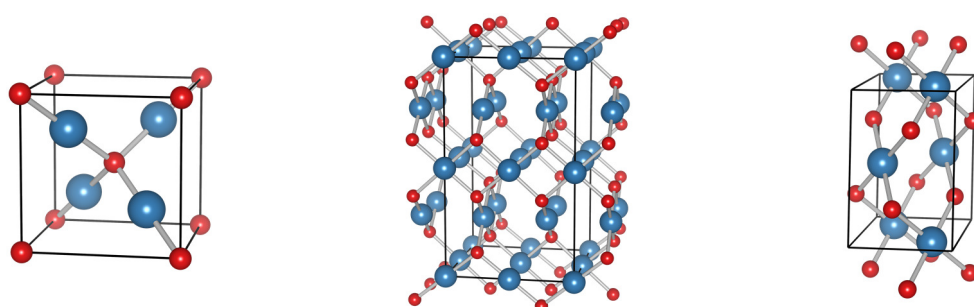
Figure 26. Crystal structure of copper oxides: Cu_2O (left), Cu_4O_3 (middle), and CuO (right). Blue coloured spheres represent copper atoms, while red coloured balls represent oxygen atoms.

Using calculations performed on the SCARF cluster with the CRYSTAL code, we have used time-dependent density functional theory (TD-DFT) to study the possible electronic excitations occurring in three copper oxides of interest: cuprous oxide (Cu_2O), cupric oxide (CuO), and paramelaconite (Cu_4O_3). Our calculations reproduce the electronic band structures of all three copper oxides accurately (Figure 276). For Cu_2O, we confirm the experimentally observed nature of the foremost transitions between the valence and conduction band as parity forbidden [3]. Cu_4O_3 and CuO are confirmed as indirect band gap semiconductors where the absorption onset is governed by strong phonon contributions. Our analysis indicates how hybrid TD-DFT is sufficient to successfully reproduce some of the excitation phenomena occurring in copper oxides.
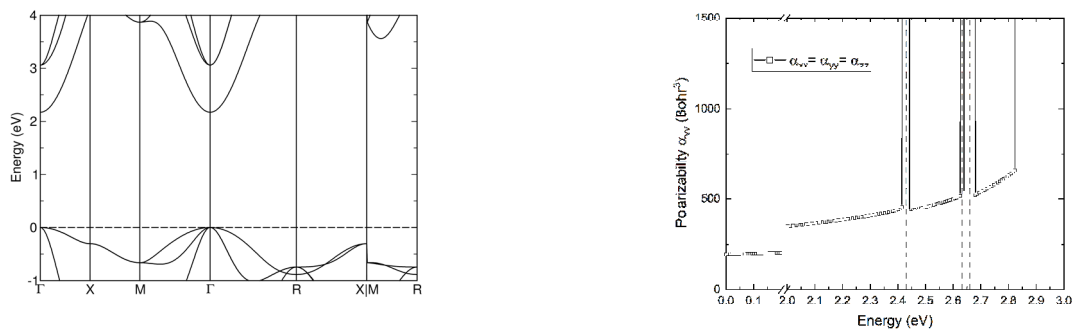
Figure 27. Calculated electronic band structure (left) and energy dependence on the diagonal components of the polarizability tensor computed using TD-B3LYP for Cu₂O (right).

References:

[1] M. Takahata and N. Naka, Phys. Rev. B 98, 195205 (2018).

[2] H. Tanimura, K. Tanimura, and P. H. M. van Loosdrecht, Phys. Rev. B 100, 115204 (2019).

[3] B. K. Meyer, A. Polity, D. Reppin, M. Becker, P. Hering, P. J. Klar, T. Sander, C. Reindl, J. Benz, M. Eickhoff, C. Heiliger, M. Heinemann, J. Bläsing, A. Krost, S. Shokovets, C. Müller, and C. Ronning, Phys. Status Solidi 249, 1487 (2012).

Probe Beam Injection into a Plasma Undulator

O. Apsimon[1,4], D. Seipt[2], Y. Ma[2], D. Jaroszynski[3,4], G. Xia[1,4], and A. G. R. Thomas[2]

1. The University of Manchester, Manchester M19 3PL, United Kingdom
2. University of Michigan, Ann Arbor MI 48109-2104, United States of America
3. University of Strathclyde, Glasgow G11XQ, Scotland
4. The Cockcroft Institute of Accelerator Science and Technology, Warrington, WA4 4AD, United Kingdom

A plasma undulator is formed when a short laser pulse is injected into a parabolic plasma channel off-axis or at an angle that causes the centroid of this laser pulse to oscillate [1-3]. Ponderomotively driven plasma wake will follow this centroid given that the product of the plasma wave number and the characteristic Rayleigh length of the laser is much larger than one. This oscillating transverse wakefield works as an undulator (wiggler) forcing particles to follow sinusoidal trajectories and emit synchrotron radiation. Theoretically, a plasma undulator can generate order of magnitude larger effective magnetic fields than conventional undulators.
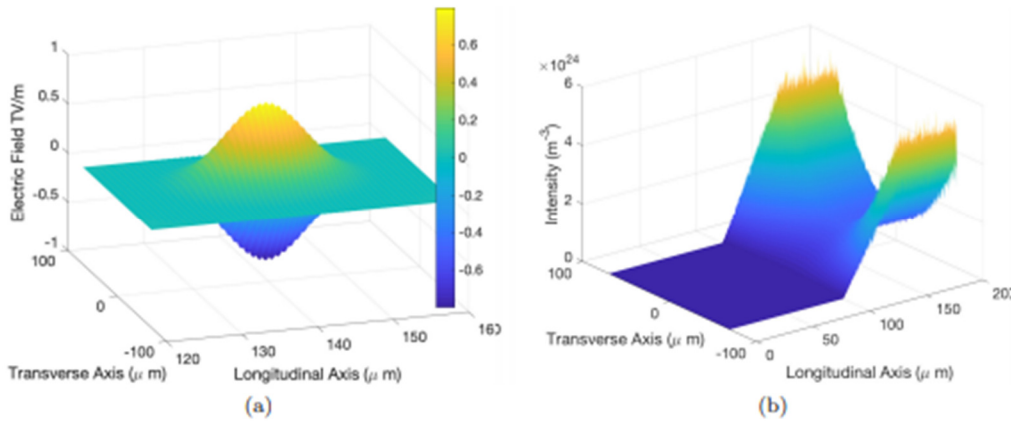
Figure 28: (a) The initial field profile of the 800 nm driver laser with a peak electric field of 0.8 TV/m and a normalised vector potential of 0.2. It is created at vacuum and focused down to a radius of 30 µm at the entrance of plasma at 180 µm. (b) The density profile of the plasma electrons for the first 200 µm of the simulation. The first 100 µm of the simulation window is a vacuum section where the laser pulse is created under the consistent Maxwell equations. This is followed by a 10 µm density up-ramp section to provide a realistic scenario then the parabolic density distribution starts with axial density of 0.425×10^{18} cm^{-3} for a dephasing length of 10 cm.
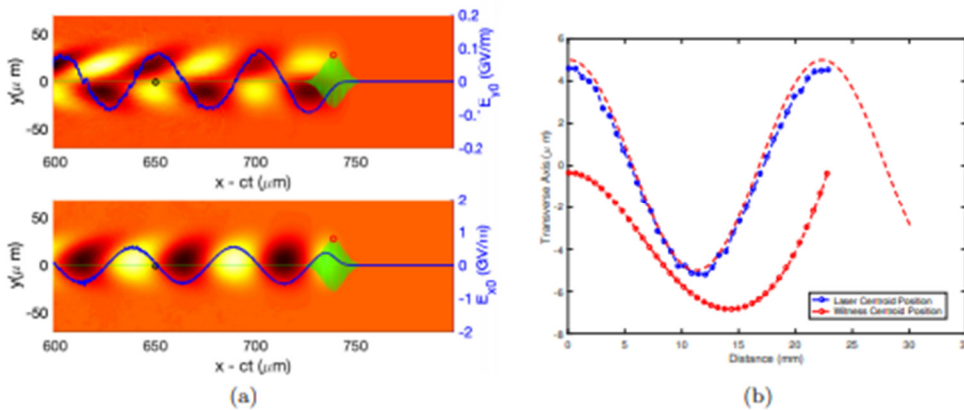
Figure 29: Results obtained by EPOCH, a UK community PIC code installed on SCARF cluster. a) Transverse and longitudinal field regions (colour map) with on axis values are shown by blue line plots. Laser pulse is depicted with green line (not to scale). The injection location of the probe electrons is denoted by a black dot where field phase is $3\pi/2$ hence the longitudinal field, $E_x = 0$,

whereas the transverse field Ey > 0. (b) The evolution of laser and probe beam centroid positions for the first oscillation wavelength, i.e., 2πZR where RZ is the Rayleigh length of the laser. This first cycle is simulated over 3 days running on 1000 cores over 100 nodes. Such studies are only possible using large scale infrastructures such as SCARF.

References:
[1] S. G. Rykovanov et al., PRL 114, 145003 (2015). 2O. Apsimon et al., Proceedings of International Particle Accelerators Conference, 1584-1586 (2017). 3S. G. Rykovanov et al., Phys. Rev. AB 19, 090703 (2016).

The blind implosion-maker: Automated inertial confinement fusion experiment design

Peter Hatfield[1] , Steven Rose[1,2], Robbie Scott[3] , Ibrahim Almosallam[4,5], Stephen Roberts[6] , Matt Jarvis[7,8]

1. Clarendon Laboratory, University of Oxford, Oxford OX1 3PU, U.K.
2. Blackett Laboratory, Imperial College London, London SW7 2AZ, U.K
3. Central Laser Facility, STFC Rutherford Appleton Laboratory, Didcot OX11 0QX, U.K.
4. King Abdulaziz City for Science and Technology, Riyadh 11442, Saudi Arabia
5. Saudi Information Technology Company, Riyadh 12382, Saudi Arabia
6. Department of Engineering Science, University of Oxford, Oxford OX1 3PJ, U.K.
7. Oxford Astrophysics, University of Oxford, Oxford OX1 3RH, U.K.
8. Department of Physics, University of the Western Cape, Bellville 7535, South Africa

We have used SCARF to begin a programme of using modern machine learning and data science tools to aide in the design of inertial confinement fusion (ICF) experiments. This requires doing large numbers of ICF simulations – only made possible by the computational and parallelisation capacities of SCARF. This work has resulted in novel designs for potential use at the National Ignition Facility (NIF), as well as opening up a completely new line of approach for designing ICF experiments. Recent challenges in achieving a high-yield implosion at the National Ignition Facility (NIF) have led to new interest in considering a much wider design parameter space than normally studied [1]. With SCARF we used a genetic algorithm to produce reasonable ICF designs with minimal assumptions [2]. We show that it takes ~5 × 104 simulations for the algorithm to find an original NIF design. We then used an advanced sparse Gaussian process-based machine learning algorithm to further refine the design produced by the genetic algorithm – in particular describing how to decompose uncertainty on predictions into uncertainty from lack of data versus uncertainty from shotto-shot variation [3]. Finally we linked these methods to other parts of the design process and looked toward a completely automated ICF experiment design process— changing ICF from an experiment design problem to an algorithm design problem.
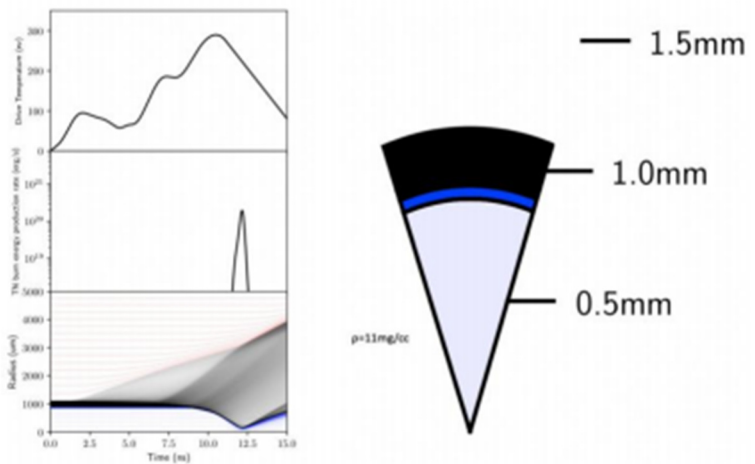
Figure 30: Taken from Hatfield et al., 2019a, the capsule design, drive shape, and implosion structure of the ICF experiment designed by the genetic algorithm

References:
[1] Peterson et al., Phys. Plasmas 24, 032702, 2017
[2] Hatfield et al., Phys. Plasmas, 26, 6, 062706, 2019
[3] Hatfield, et al., IEEE Transactions on Plasma Science, DOI: 10.1109/TPS.2019.2944416, 2019

Muon quantum effects within an anharmonic approach

Ifeanyi John Onuorah, Pietro Bonfà, Muhammad Maikudi Isah, Roberto De Renzi

Department of Mathematical, Physical and Computer Sciences, University of Parma, Italy

Density functional theory (DFT) calculations of the muon implantation sites and of its interaction (within the Born-Oppenheimer (BO) approximation) usually treat the muon as a point impurity, ignoring the effects of the muon zero point vibrational energy. However, the zero point vibrational energy can play a role in stabilizing the implantation sites in host materials and in the quantitative estimation of the hyperfine interactions and other physical observables[1].

As a first-order correction, the muon zero-point motion is usually described within the harmonic approximation, despite the anharmonicity of the crystal potential. In collaboration with the authors of the "stochastic self-consistent harmonic approximation (SSCHA)" [2,3], we have specialized this approach to the muon case to provide an accurate ab-initio description of the quantum nature of the muon. The SSCHA is a quantum variational method that efficiently calculates anharmonic free energies and phonon frequencies in a non perturbative way. For the muon, the SSCHA is variational in the muon (free) energy, with this energy evaluated stochastically from forces and energies calculated using the DFT (performed on SCARF) at a sufficient number of random muon configurations. The muon energy is minimized using trial harmonic wave functions that are Gaussian, while the minimization parameter is the width of the Gaussian.
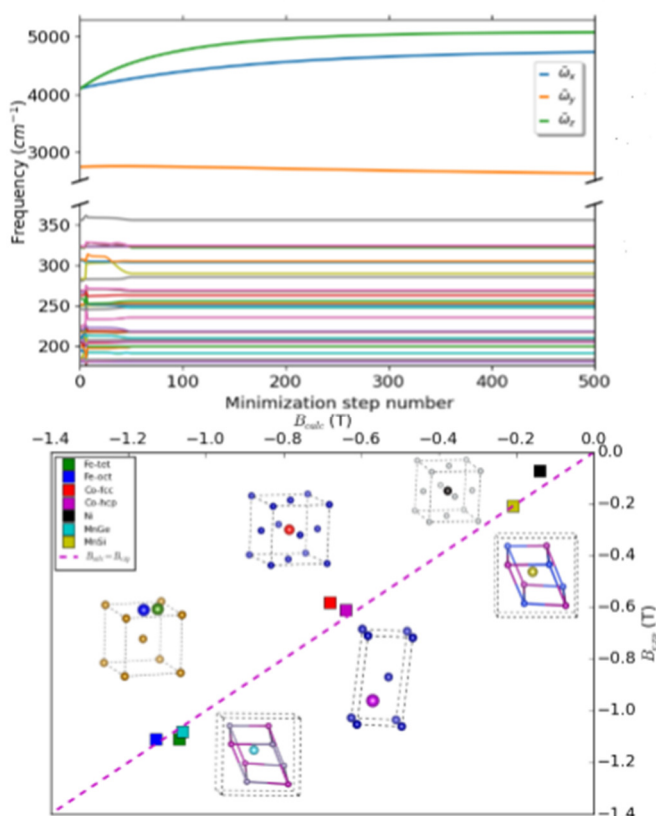
Figure 31: Evolution of the SSCHA muon frequency ($\tilde{\omega}$ in the lower panel) and those of Fe (nearly static low-frequency lines in the lower panel) during minimization for the muon in the tetrahedral site of bcc Fe. The figure depicts the expected anharmonicity effects on the SSCHA muon frequencies and nearly non-existent anharmonicity effects on those of Fe, due to the large mass difference of the muon and Fe nuclei[1]

We further used the SSCHA muon wave function to refine the contact hyperfine field in a series of metals: Fe, Ni, Co, MnSi and MnGe, where the SSCHA improves the agreement

of the calculated value (Bcalc) with the experimental results (Bexpt) (see figure on the left) with respect to recent point impurity calculations[4] . Finally, the quantum treatment within the SSCHA allows the stable occupation of the muon at the octahedral site in bcc Fe, which is unstable within the harmonic regime.

We have also continued to use DFT calculations performed on SCARF to search for possible muon implantation sites in selected materials including Fe2P, EuCoGe and V3Ge.

References:
[1] I. J. Onuorah, P. Bonfà, R. De Renzi, et. al Phys. Rev. Materials 3, 073804 (2019)
[2] I. Errea et. al Phys. Rev. Lett. 111, 177002 (2013).
[3] L. Monacelli et al Phys. Rev. B. 98, 024106 (2018).
[4] I. J. Onuorah, P. Bonfà, R. De Renzi, Phys. B 97, 174414 (2018)

Structure and spectroscopy of the supercapacitor material hydrous ruthenium oxide, RuO$_2$.xH$_2$O, by neutron scattering

Stewart F Parker[1], Stephen J. Robertson[2] and Silvia Imberti[1]

1. *ISIS Facility, STFC Rutherford Appleton Laboratory, Chilton, Didcot, OX11 0QX, UK*
2. *Advanced Material Group, STFC Rutherford Appleton Laboratory, Chilton, Didcot, Oxfordshire, OX11 0QX, UK*

This work has been published in Molecular Physics[1]

Supercapacitors (also called electric double-layer capacitors or ultracapacitors) **are** energy storage devices with very high capacity and a low internal resistance. They consist of two electrodes, an electrolyte, and a separator which isolates the two electrodes electrically. The mechanism of energy storage is a simple charge separation at the interface between the electrode and the electrolyte. The key component is the electrode material. Hydrous ruthenium dioxide, RuO$_2$.xH$_2$O, is a material of active investigation as an electrode material for this application. A combination of elastic (ND) and inelastic neutron scattering (INS) together with thermal gravimetric studies and DFT calculations performed on SCARF, have provided new insight into the nature of the surface species present on RuO$_2$.xH$_2$O. Our ND results confirm that hydrous ruthenium oxide is a nanocrystalline material consisting of a core of RuO$_2$. The INS results show that the surface consists largely of Ru–OH with small amounts of water hydrogen-bonded to the surface. To gain insight into the likely surface structures, we have investigated, computationally, nine possible structures. Comparison of observed and calculated INS spectra is a stringent test of a model. The model that showed the best agreement is shown in Figure 32 (left), (the comparison of observed and calculated spectra are shown in the right hand side part), and consists of hydrogen-bonded Ru–O–H oriented along [001] *i.e.* parallel to the surface bridging oxygen atom. The hydroxyls are stable up to ~200 °C, *i.e.* over the composition range $x = 0.2 – 2$. The optimal supercapacitor material has $x = 0.5 – 0.7$, and in this range the surface is fully hydroxylated. This provides a ready route for the proton transport: a proton can attach to a surface hydroxyl to generate coordinated water, proton transport then occurs along the hydrogen-bonded chain by a Grotthuss-type hopping mechanism.
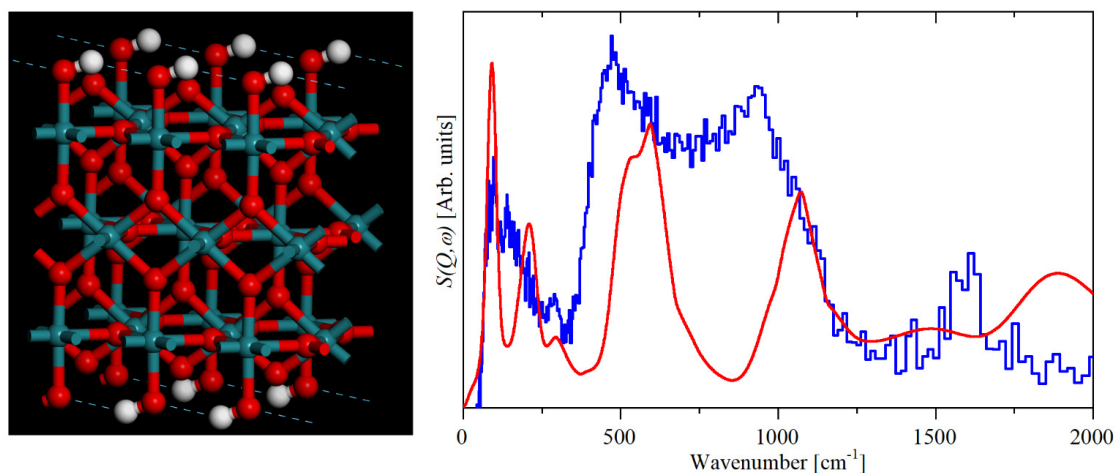
Figure 32: (Left) the model that best accounts for the INS spectra. (Dark green = ruthenium, red = oxygen, white = hydrogen, dashed blue lines indicate hydrogen-bonds). (Right) INS spectrum of RuO2.0.99H2O, (blue) and the spectrum generated from the model shown on the left (red).

References:
[1] S.F. Parker, S.J. Robertson and S. Imberti, *Molecular Physics* (2019). [doi: 10.1080/00268976.2019.1649491]

4. APPENDIX A: SCARF HARDWARE DETAILS

Host group	CPU	Nodes	Cores /node	Total cores	Interconnect	Total mem (GB)
SCARF 18	Intel Xeon Gold 6126	148	24	3552	EDR Infiniband	28416
SCARF 17/ DeRevolutionIbus	Intel E5-2650 v4	201	24	4824	EDR Infiniband	25728
SCARF 16/ MagnaCarta/ IBIS	Intel E5-2650 v3	56	20	1120	FDR Infiniband	7168
SCARF 15	Intel E5-2650 v3	68	20	1360	FDR Infiniband	8704
SCARF 14	Intel E5-2650 v2	56	16	896	QDR Infiniband	7168
GPU 17	Intel E5-2623 v3	5	8	40	FDR Infiniband	640
GPU 15	Intel E5-2623 v3	4	8	32	FDR Infiniband	512
GPU 14	Intel E5-2623 v3	8	8	64	FDR Infiniband	1024
GPU 13	Intel E5-2650 v2	12	8	86	FDR Infiniband	768
Total		**558**		**11,974**		**80,128**

5. APPENDIX B: PUBLICATIONS AND PRESENTATIONS

Publications

	Title	Authors	Journal
1	Local Coordination in Metal-Organic Frameworks Probed in the Vibrational and Optical Regime by EELS	Sean M. Collins, Demie M. Kepaptsoglou, Keith Butler, Louis Longley, Jingwei Hou, Thomas D. Bennett, Quentin Ramasse, Paul Midgley	Microscopy and Microanalysis 25 (S2), 606-607, 2019
2	Subwavelength Spatially Resolved Coordination Chemistry of Metal–Organic Framework Glass Blends	Sean M. Collins, Demie M. Kepaptsoglou, Keith T. Butler, Louis Longley, Thomas D. Bennett, Quentin M. Ramasse, and Paul A. Midgley	Journal of the American Chemical Society 140 (51), 17862-17866, 2018
3	Understanding vibrational entropy with neutrons and high-performance computing	K. Butler, D. Bodeshiem	Chemistry of Materials 31 (20), 8366-8372, 2019
4	Understanding vibrational entropy with neutrons and high-performance computing	K. Butler, D. Bodeshiem	Journal of the American Chemical Society 141 (26), 10504-10509, 2019
5	Understanding vibrational entropy with neutrons and high-performance computing	K. Butler, D. Bodeshiem	Chemistry of Materials 30 (24), 8782-8788, 2018
6	Understanding vibrational entropy with neutrons and high-performance computing	K. Butler, D. Bodeshiem	Angewandte Chemie International Edition 57 (29), 8932-8936, 2018
7	Questaal: a package of electronic structure methods based on the linear muffin-tin orbital technique	D. Pashov et al.,	Computer Physics Communications (2019), https://doi.org/10.1016/j.cpc.2019.107065.
8	Hund's coupling mediated colossal increment in Tc in multiband FeSe manifold.	S. Acharya, et al.	arXiv preprint arXiv:1908.08136 (2019) (under review).
9	Emergence and suppression of superconductivity in the	S. Acharya, et al.	(under review).

	uncollapsed and collapsed tetragonal phases of LaFe2As2 and CaFe2As2		
10	Evening out the spin and charge parity to increase Tc in Sr2RuO4	S. Acharya, et al.	Commun Phys 2, 163 (2019). https://doi.org/10.1038/s42005-019-0254-1.
11	Vibrational dynamics of 4-fluorobenzaldehyde from periodic DFT calculations	P. Ribeiro-Claro, P. D. Vaz, M. M. Nolasco, C. F. Araujo, F. P. S. C. Gil, A. M. Amado	Chem. Phys. Lett. X, 2 (2019) 100006. DOI: 10.1016/j.cpletx.2019.10000
12	Quantum effects in muon spin spectroscopy within the stochastic self-consistentharmonic approximation	I. J. Onuorah, P. Bonfà, R. De Renzi, L. Monacelli, F. Mauri, M. Calandra, and I. Errea	Phys. Rev. Materials 3, 073804 (2019)
13	Structure and spectroscopy of the supercapacitor material hydrous ruthenium oxide, RuO2.xH2O, by neutron scattering	S.F. Parker, S.J. Robertson and S. Imberti	Molecular Physics (2019). [doi: 10.1080/00268976.2019.1649491]
14	Characterisation of *fac*-tris[2-phenylpyridinato-C^2,*N*]iridium(III) by inelastic neutron scattering spectroscopy and periodic density functional theory	S.F Parker	Journal of Physics Communications 3 (2019) 065010. [doi: 10.1088/2399-6528/ab2921]
15	Adsorbed states of hydrogen on platinum: a new perspective	S.F. Parker, S. Mukhopadhyay, M. Jiménez-Ruiz and P.W. Albers	*Chemistry—A European Journal* 25 (2019) 6496 – 6499. [doi:10.1002/chem.201900351]
16	Spectroscopic characterisation of centropolyindanes	S.F Parker, L. Zhong, M. Harig and D. Kuck	*Physical Chemistry Chemical Physics 21 (2019) 4568-4577. [doi: 10.1039/C8CP07311B]*
17	Structure and vibrational spectroscopy of methanesulfonic acid	L. Zhong and S.F. Parker	*Royal Society Open Science* 5 (2018) 181363. [doi: 10.1098/rsos.18163]
18	Synthesis, computational studies, inelastic neutron scattering, infrared and Raman spectroscopy of ruthenocene	S.F. Parker and I.R. Butler	*European Journal of Inorganic Chemistry* 2019 (2019) 1142-1146. [doi: 10.1002/ejic.201800914]

19	Comprehensive vibrational spectroscopic characterisation of Nylon-6 precursors for precise tracking of the Beckmann rearrangement	S. Chapman, A.J. O'Malley, S.F. Parker and R. Raja	*ChemPhysChem* 19 (2018) 3196-3203. [doi: 10.1002/cphc.201800721]
20	Deactivation of a single-site gold-on-carbon acetylene hydrochlorination catalyst: An X-ray absorption and inelastic neutron scattering study	G. Malta, S. Kondrat, S. Freakley, C. Davies, S. Dawson, X. Liu, L. Lu, K. Dymkowski, F. Fernandez-Alonso, S. Mukhopadhyay, E. Gibson, P. Wells, S.F. Parker, C. Kiely and G. Hutchings	*ACS Catalysis* 8 (2018) 8493–8505. [doi: 10.1021/acscatal.8b02232]
21	Complete assignment of the vibrational spectra of borazine: the inorganic benzene	S.F. Parker	*RSC Advances* 8 (2018) 23875-23880
22	Spectroscopic characterisation of model compounds, reactants and byproducts connected with an isocyanate production chain	E.K. Gibson, J. Callison, J.M. Winfield, R.H. Carr, A. Eaglesham, A. Sutherland, S.F. Parker and D. Lennon	*Industrial & Engineering Chemistry Research* 57 (2018) 7355–7362. [doi: 10.1021/acs.iecr.8b00853]
23	Catalytic performance of bulk and colloidal Co/Al layered double hydroxide with Au nanoparticles in aerobic olefin oxidation	S. R. Leandro, C. I. Fernandes, A. S. Viana, A. C. Mourato, P. D. Vaz, C. D. Nunes	*Applied Catal. A: Gen., 584 (2019), 117155.* *DOI: 10.1016/j.apcata.2019.117155*

Presentations

	Conference	Title	Presenter
1	Material and molecular modelling conference and users meeting. UCL 2019		K. Butler
2	United Kingdom Catalysis Conference, Loughborough University 2019		K. Butler
3	Theoretical and Experimental Magnetism Meeting (TEMM) 2019 and	(Invited talk) Role of non-local correlations and vertex	S. Acharya

	UK-China Workshop on Strongly Correlated Electron Systems, Abingdon, Oxfordshire (UK).	corrections in magnetic susceptibilities	
4	Questaal Workshop, Daresbury, May 2019 (UK)	From why DMFT? to why not DMFT!	S. Acharya
5	APS March Meeting 2019	Spin-charge co-operation in even-parity three dimensional nodal superconductivity in strained Sr2RuO4	S. Acharya
6	FCMP 2020, Bristol, UK	Evening out the spin and charge parity to increase Tc in Sr2RuO4	S. Acharya
7	2019 Fall Meeting of the European Materials Research conference	Computational Analysis of the LiNH2-Li2NH Solid Solution	E. Chadwick, L. Liborio, S. Sturniolo
8	FEBS Advanced Lecture Course 2019 Biological Surfaces and Interfaces: The Mechanistic View, San Feliu del Guixols. Spain, June 30- July 5, 2019,	Book of Abstracts (Poster) Molecular Dynamics of Water in Model Phospholipid Membranes: Studying the effect of water model	J.Á. Martínez-González, V. Garcia-Sakai
9	XXXVII Biennial Meeting of the Royal Spanish Society of Chemistry, San Sebastian. Spain, May 26-30, 2019	Book of Abstracts (Poster) Molecular Dynamics of Water in Models Phospholipid Membranes: Effect of water model	J.Á. Martínez-González, V. Garcia-Sakai
10	ISIS Molecular Spectroscopy Science Meeting, University College London, London, UK, November 6-7, 2018.	(Poster) Project - Understanding the Interface between Water and biomaterials: Combining Neutron Scattering and in-silico studies	J.Á. Martínez-González
11	Erice School on Neutron Science and Instrumentation, "Neutrons for Chemistry and materials Science Applications"	Vibrational Spectroscopy with Neutrons: Direct Geometry Instruments	S.F. Parker

12	ILL-ESS User Meeting, Grenoble, 10th October 2018	*Operando* neutron spectroscopy: lessons learned and opportunities	S.F. Parker
13	ILL-ESS User Meeting, Grenoble, 10th October 2018	Characterisation of the surface species on carbon supported Pd catalysts	S.F. Parker
14	Cardiff Catalysis CDT/MSc Student Visit to ISIS	What neutrons can do for catalysis	S.F. Parker
15	ACS Spring Meeting, Orlando, 31st March 2019	Characterisation of the surface species on carbon supported Pd and Pt catalysts	S.F. Parker
16	Oxford School of Neutron Scattering	Vibrational spectroscopy with neutrons: inelastic neutron scattering (INS)	S.F. Parker
17	University of Glasgow, MRes in Heterogeneous Catalysis	Neutrons and catalysis: Introduction to neutron scattering	S.F. Parker
18	University of Glasgow, MRes in Heterogeneous Catalysis	Neutrons and catalysis: INS studies of catalyst activation and deactivation	S.F. Parker
19	Highgate School	What have neutrons done for me?	S.F. Parker
20	Efficient neutron Sources workshop, 2-5 September 2019- PSI Auditorium, Villigen/Zurich Switzerland	Advanced neutron tracking for the upgraded TS1-TRAM at ISIS: a roadmap toward the enhancement of the signal to noise ratio at the instrument sample location	L. Quintieri

6. APPENDIX C: SCARF QUEUE USAGE 2018-19

General SCARF Queues

Unsurprisingly, of the non-restricted queues, usage of the *scarf* queue dominates. The *preemptable* queue allows users to run across all hardware (including that which is normally restricted) with the caveat that the job may be ended if the nodes are required by a job in another queue that the hardware normally prioritises. The *devel* queue is intended for short interactive workloads. Uptake of these queues, which were introduced last year, has been slow. It is possible that this is due to them not being publicised enough and that increased awareness of their specific purposes may encourage their use. The reporting period also includes the final few months that the scarf-rhel7 queue was in operation.
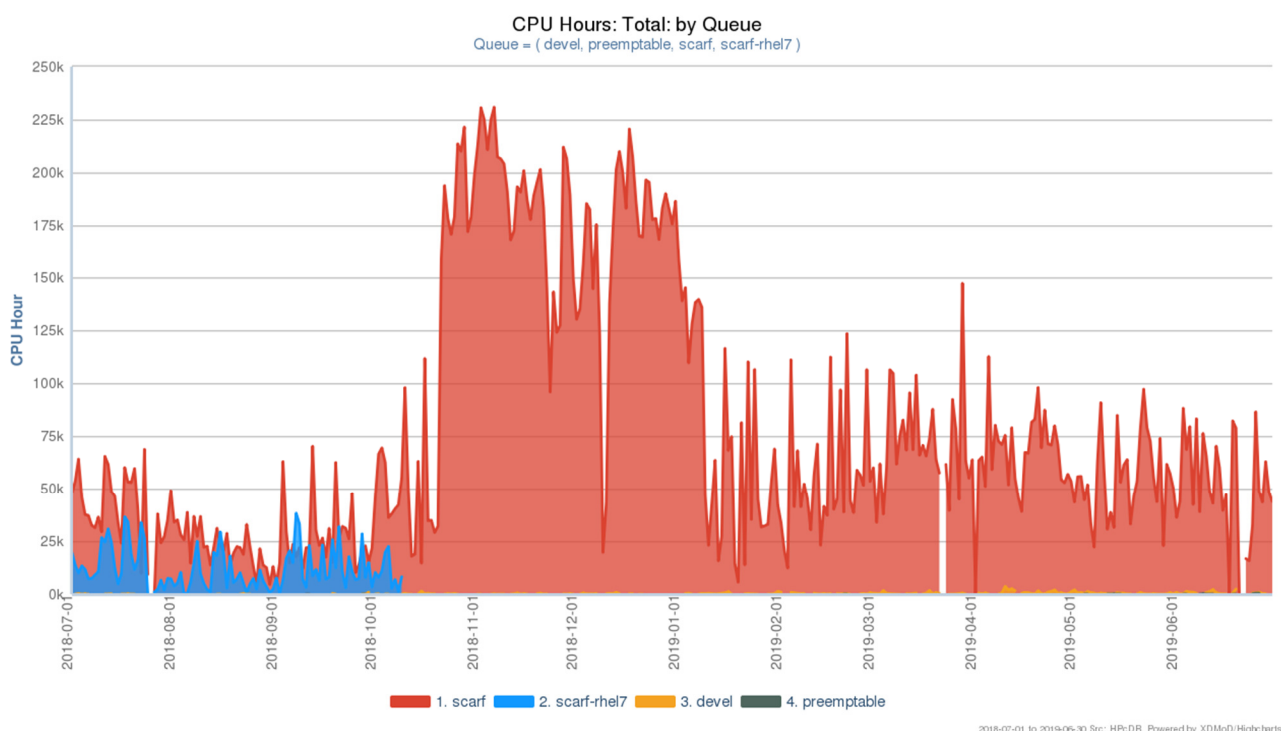
Figure 33: SCARF Queue Usage

MagnaCarta, DeRevolutionibus and Lexicon2 Queues

These queues are primarily for CLF Plasma Physics use. MagnaCarta has 480 cores purchased in 2016. DeRevolutionibus has 1608 cores purchased in 2017. Lexicon2 had 544 cores purchased in 2010, but was decommissioned with the move to Slurm.
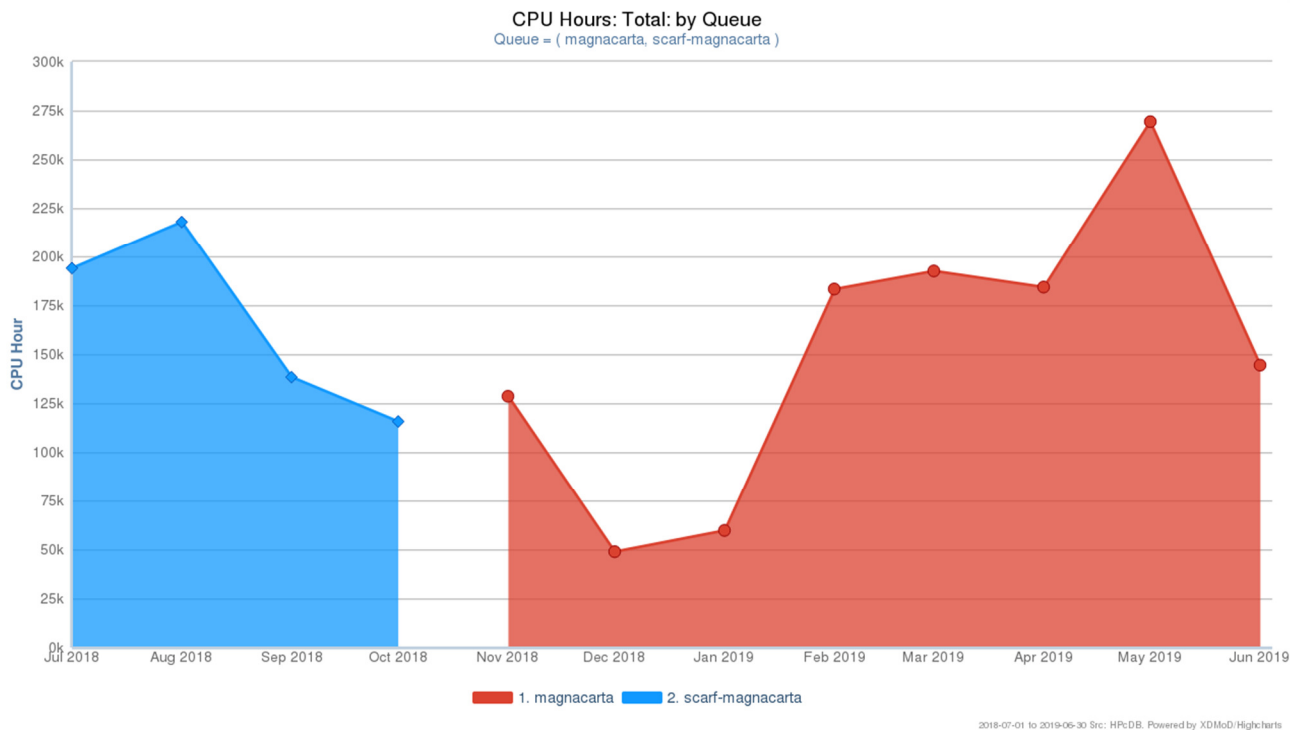
Figure 34: SCARF-MagnaCarta Usage

The graph for the SCARF-MagnaCarta queue shows significant usage, as it is available to CLF external collaborators.
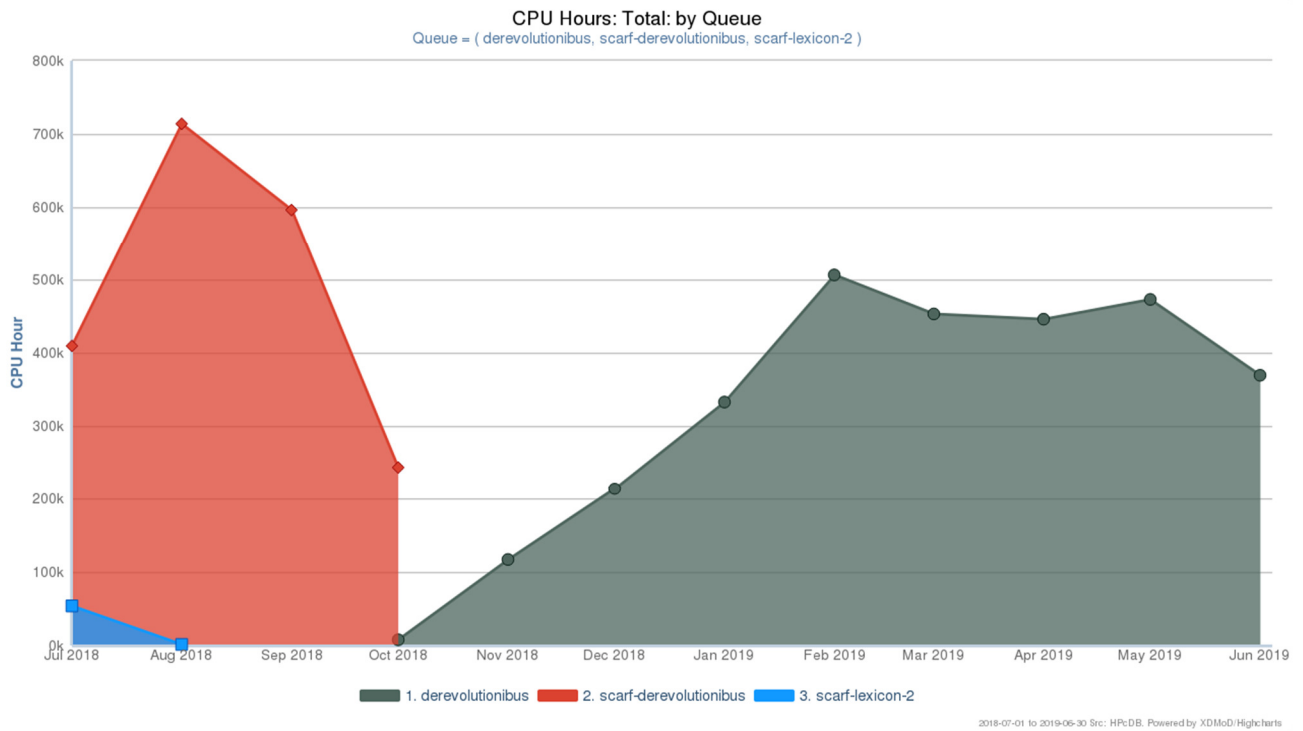
Figure 35: SCARF Lexicon-2 and DeRevolutionIbus Usage

DeRevolutionibus continues to be used for higher priority MagnaCarta users and on demand to support CLF experiments. The SCARF-Lexicon-2 queue was retired in August.

SCARF-IBIS

SCARF-IBIS has a capacity of 240 CPU cores and are used for the *Intense Beams in Synchrotrons* collaboration.
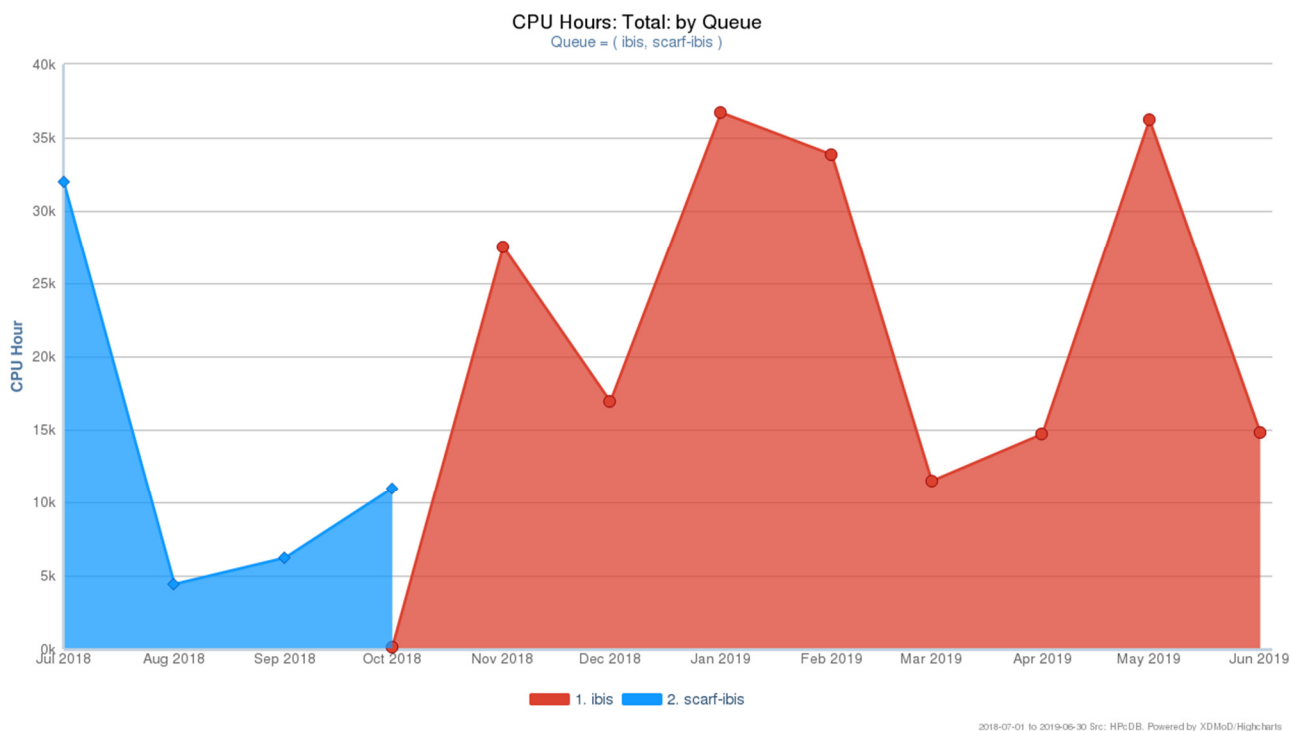
Figure 36: SCARF-IBIS Usage

SCARF Total Power draw
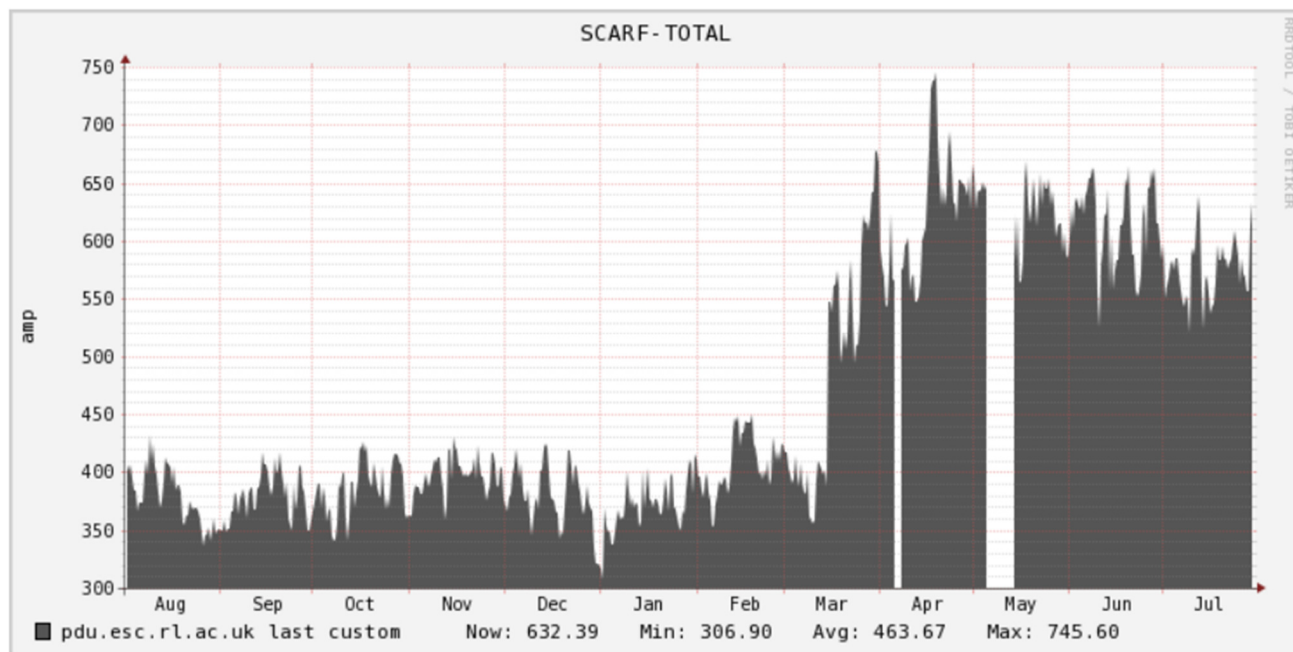
Figure 37: SCARF Power Usage

In the graph above, the uptake of the SCARF18 hardware and its impact on power draw can be clearly seen. There are two interruptions to the graph which were due to monitoring issues and were not service outages. The approximate average power draw of the SCARF cluster for the period was 453 amps or 108 kW, excluding the power needed to cool, pump and move cold air.

Year Purchased	Gflops/W
2013	0.59
2014	0.98
2015	1.95
2016	1.95
2017	2.05
2018	3.05

Figure 38: GFlops/W for SCARF generations of equipment

From the above table it is clear that the Gflops/W achieved increase per generation of the SCARF equipment. This supports the continual refresh rate of SCARF hardware rather than a big bang approach. SCARF16 is the same hardware as SCARF15 which accounts for the identical Gflops/W.

Filesystem Usage

The plot below outlines the use of the Panasas filespace on the SCARF service. The new storage system has significantly increased capacity.
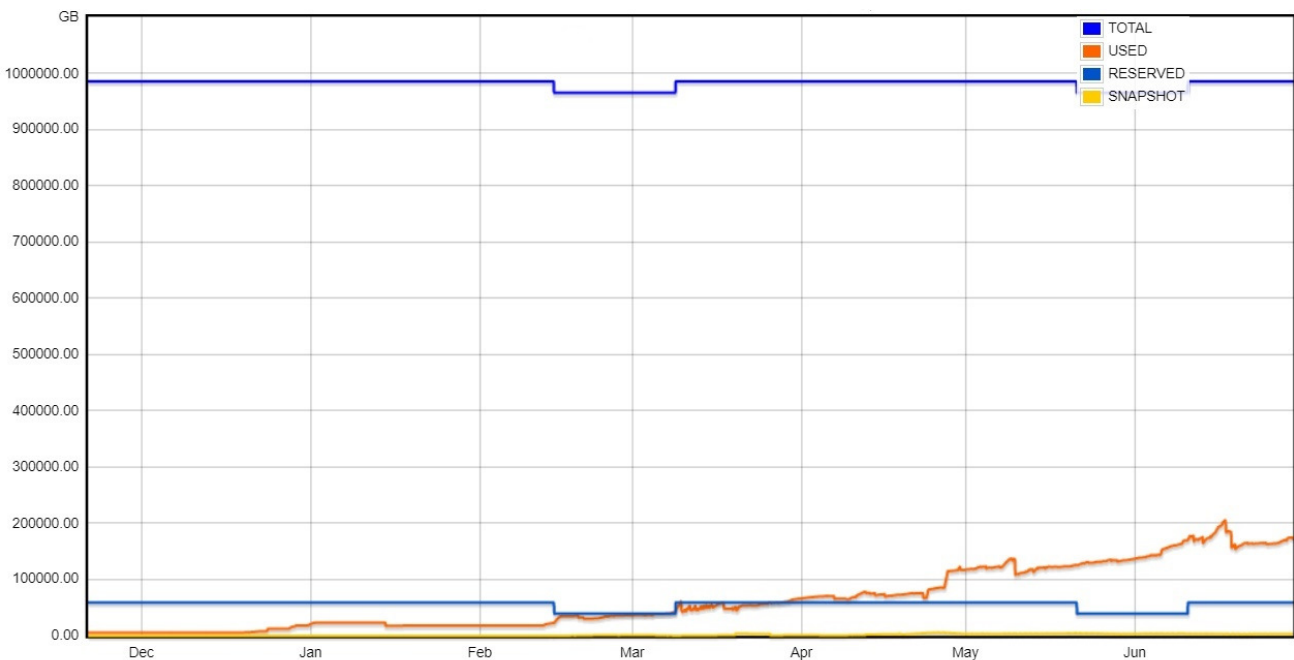
Figure 39: Filespace usage on the Panasas Storage

Networking

The diagram below shows the SCARF compute clusters embedded in the larger Research Infrastructure group's networking infrastructure. The only significant change this year was the removal of the old Panasas storage system (panfs2).
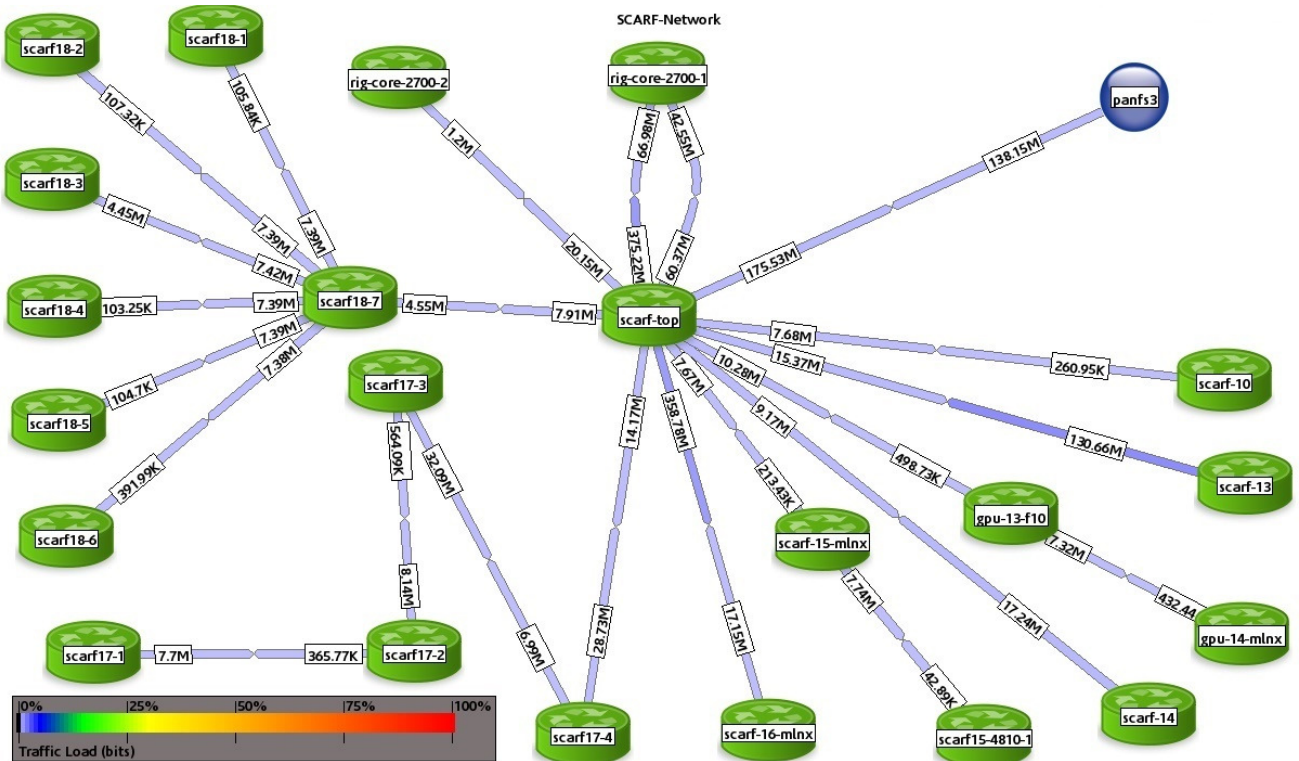
Figure 40: SCARF Network Topology

APPENDIX D: SCARF DEVELOPMENTS

Once again, it has been a busy year for the SCARF service. Users will have predominately noticed the addition of a third head node and upgrades to many of the applications and libraries however much effort goes into improving the management of SCARF in ways that are not immediately obvious.

Technical Developments

- The latter part of the year saw the completion of the migration from RHEL6 and the move to SLURM
- SCARF10,11,12 and 13 were decommissioned and removed from the racks
- A new physical login node named ui4.scarf.rl.ac.uk was put into service
- A 2PB, Infiniband-connected GPFS volume was commissioned to provide a fast scratch area for the K80 GPU nodes

Easybuild

The Easybuild 'software build and installation framework' was adopted as the dominant mechanism for the delivery of applications software, libraries and supporting utilities. Previously this was compiled manually or by using custom shell scripts. The use of Easybuild will reduce the time it takes to install and update the more common software packages when they are requested by users. Additionally, it will ensure reproducibility and minimise dependency incompatibility.

Storage Migration

By far the most significant development this year was the migration of all user data to the new Panasas instance.

Panasas underpins almost all of SCARF's storage areas including the home directories and the work and scratch areas. In addition to increasing capacity from 370TB to approximately 1PB, SCARF's new Panasas installation added SSDs to the existing traditional hard disks, providing faster access to file meta-data.

It was important that no writes were performed to data while being migrated so a schedule was devised and users were informed of their migration date in advance. Most of the data had been moved already so that a 'final synchronisation' was all that was needed, which kept disruption to individual users to a minimum. The old Panasas system was retained for a period before being decommissioned.

Changes to established practices

- Memory limits were introduced as after the migration to SLURM we frequently saw jobs being terminated due to using all the memory on the node.
- A new module area for Easybuild-generated software was introduced

Application Stack

A selection of new or updated applications is in the table below:

Application	Area	Version
VSim	VSim is a multi-physics simulation tool	10.1.0
NAMD	Molecular dynamics simulation	2.13
OpenMPI	Open source Message Passing Interface implementation	3.13
GAUSSIAN	Computational chemistry	16 Rev. B.01

A full list of the available software on SCARF can be found on the SCARF website: https://www.scarf.rl.ac.uk/scarf_apps.html.

7. APPENDIX E: INDEX OF FIGURES